Cell-to-cell signalling mediated via CO_2: activity dependent CO_2 production in the axonal node opens Cx32 in the Schwann cell paranode.

Jack Butler[1], Lowell Mott[1], Angus Brown[2] and Nicholas Dale[1*]

[1]School of Life Sciences
University of Warwick
Coventry, CV4 7AL

[2]The University of Nottingham Medical School
Queen's Medical Centre
Nottingham, NG7 2UH

*Author for correspondence: N.E.Dale@warwick.ac.uk

Abstract

Loss of function mutations of Cx32, which is expressed in Schwann cells, cause X-linked Charcot Marie Tooth disease, a slowly progressive peripheral neuropathy. Cx32 is thus essential for the maintenance of myelin. During action potential propagation, Cx32 hemichannels in the Schwann cell paranode are thought to open and release ATP. As Cx32 hemichannels are directly sensitive to CO_2, we have tested whether CO_2 produced in the axonal node, as a consequence of the energetic demands of action potential propagation, might gate Cx32 hemichannels. Using isolated sciatic nerve from the mouse, we have shown that the critical components required for intercellular CO_2 signalling are present (nodal mitochondria, the source of CO_2; a CO_2-permeable aquaporin, AQP1; paranodal Cx32; and carbonic anhydrase). We have used a membrane impermeant fluorescent dye FITC, which can permeate Cx32 hemichannels, to demonstrate the opening of Cx32 in Schwann cells in response to an external CO_2 stimulus or during action potential propagation in the isolated nerve. Pharmacological blockade of APQ1 or allosteric enhancement of carbonic anhydrase activity greatly reduced Cx32 gating during action potential firing. By contrast, inhibition of carbonic anhydrase with acetazolamide greatly increased Cx32 gating. Cx32 gating was unaffected by the G-protein blocker GDPβS, indicating that it was not mediated by G protein coupled receptors. This CO_2-dependent opening of Cx32 also mediates an activity dependent Ca^{2+} influx into the paranode and, by increasing the leak current across the myelin sheath, slows the conduction velocity. Our data demonstrate that CO_2 can act via connexins to mediate neuron-to-glia signalling and that CO_2 permeable aquaporins and carbonic anhydrase are key components of this signalling mechanism.

Introduction

Connexin32 (Cx32) is expressed in Schwann cells and oligodendrocytes, the myelinating cells of the peripheral and central nervous system, respectively. These cells wrap around axons to form the myelin sheath, an insulating barrier that restricts voltage dependent ion fluxes to the nodes of Ranvier, thus enabling saltatory conduction (Huxley and Stampfli, 1949). Charcot Marie Tooth (CMT) disease is a slow progressing peripheral neuropathy that involves a loss of peripheral myelin integrity (Murakami et al., 1996). Typical symptoms of CMT include slowing of peripheral conductance velocity, loss of feeling in the extremities, *pes cavus* and in some cases muscle wasting. Mutations in the *gjb1* gene, encoding Cx32, result In the X linked version of CMT (CMTX) (Bergoffen et al., 1993; Fairweather et al., 1994; Hattori et al., 2003; Record et al., 2023). *Cx32*-null mice reproduce CMTX phenotypes, indicating CMTX is caused by a loss of Cx32 function (Scherer et al., 1998). This phenotype can be rescued by selective re-expression of Cx32 in Schwann cells, highlighting how fundamental Cx32 is to the maintenance of myelin health (Scherer et al., 2005).

Cx32 is a β connexin and is closely related to Cx26 and Cx30. Hemichannels of these connexin isoforms can be opened by increases in PCO_2, at constant extracellular pH and physiological concentrations of Ca^{2+} (Huckstepp et al., 2010; Meigh et al., 2013; Dospinescu et al., 2019; Butler and Dale, 2023). CO_2 sensitivity of these β connexins is dependent on a "carbamylation motif" (Meigh et al., 2013; Brotherton et al., 2022; Brotherton et al., 2024; Nijjar et al., 2025). While the mechanism of CO_2 sensitivity has been most thoroughly studied in Cx26, Cx32 possesses the same carbamylation motif that is required for CO_2 sensitivity (Dospinescu et al., 2019; Butler and Dale, 2023). In Cx32, CO_2 carbamylates the primary amine of Lys124 in the motif. As this carbamylated amine is now negatively charged, it can form a salt bridge with Lys104 of the neighbouring subunit. The resulting carbamate bridges are thought to bias the hemichannel to the open state. Like most connexins, Cx32 will form gap junction channels where two hexamers of Cx32 in opposing membranes can dock together. Cx32 gap junction channels, however, are insensitive to the changes in PCO_2 that can open Cx32 hemichannels (Dospinescu et al., 2019).

Myelin expresses Cx32 as both unopposed hemichannels in the paranodal membrane and also as reflexive gap junctions in the Schmidt Lanterman incisures (Bergoffen et al., 1993; Meier et al., 2004; Bortolozzi, 2018). The reflexive gap junctions provide radial diffusion pathways through the layers of myelin. However, radial diffusion pathways still exist in *Cx32*-null mice, suggesting a mechanism of redundancy or compensation (Balice-Gordon et al., 1998). Nevertheless, as *Cx32*-null mice still reproduce CMTX (Scherer et al., 1998), the loss of Cx32 hemichannel function must be sufficient to induce CMTX pathology.

Cx32 hemichannels in the paranode are thought to gate open and release ATP during action potential propagation (Nualart-Marti et al., 2013). The mechanism underlying the opening of Cx32 hemichannels in the paranode in response to action potential propagation remains uncertain. Two hypotheses have been proposed: i) because Cx32 is intrinsically voltage sensitive, hemichannel opening could be caused by transmembrane potential excursions during action potential propagation (Abrams et al., 2002); and ii) a rise in intracellular Ca^{2+} within the Schwann cell paranode possibly downstream of activation of a G-protein coupled receptor could open Cx32 (Carrer et al., 2018).

In this paper we explore an alternative hypothesis: that CO_2, produced in the node as a consequence of the energetic demands of restoring transmembrane ionic gradients following

action potential propagation (via Na^+/K^+ ATPases), diffuses into the paranode to open Cx32. We have tested our hypothesis by careful consideration of the requirements of a CO_2-based signalling system: a means of production (mitochondria); a channel to allow CO_2 produced in the node to diffuse into the paranode as CO_2 does not readily cross biological membranes; and a mechanism to terminate the actions of CO_2 (carbonic anhydrase). We show that all of these components are present at the node/paranode and that their manipulation will alter the gating of Cx32 in ways that support our hypothesis.

Results

The components for CO_2 signalling mediated via Cx32 are present in myelin

A CO_2-based signalling system in myelin requires: a means of production; a channel to allow CO_2 to cross the nodal and paranodal membranes; and a mechanism to terminate the actions of CO_2 (Fig 1). It is already known that: mitochondria are present in the node (Ohno et al., 2011); Cx32 is expressed in the paranode (Bergoffen et al., 1993); AQP1, highly permeable to CO_2 (Endeward et al., 2006; Musa-Aziz et al., 2009), is expressed in Schwann cells (Gao et al., 2006; Segura-Anaya et al., 2015); and carbonic anhydrase is universally present in every cell. Here we have used high resolution microscopy to examine the precise subcellular localisation of these components relative to each other.

Mitochondria localise to the axonal node and Schwann cell paranode and may be brought in close proximity to Cx32 via SFXN1

SFXN1 is a mitochondrial protein that also binds to Cx32 (Fowler et al., 2013). Using cytochrome C (CytC), as a mitochondrial marker we found that mitochondria were localised in both the axonal node and Schwann cell paranode (Fig 2, Fig 2 fig supplement 1), in accordance with previous reports (Rydmark et al., 1998; Ohno et al., 2011). There was colocalization between Cx32 and CytC in the Schwann cell paranode, and (Fig 2, mean; 95% confidence interval, M1: 0.314; 0.198, 0.431 and M2: 0.261; 0.165, 0.357). There was also colocalization in the Schwann cell paranode between CytC and SFXN1 (Fig 2, M1: 0.568; 0.441,0.695 and M2: 0.462; 0.336, 0.588). This suggests that SFXN1 may facilitate the association of Cx32 and mitochondria (Fowler et al., 2013). Interestingly, SFXN1 was also observed in the absence of CytC (Fowler et al., 2013) suggesting that it has additional cellular roles unrelated to its mitochondrial function.

AQP1 is present in the axonal node and Schwann cell paranode

AQP1, a CO_2 permeable aquaporin (Endeward et al., 2006; Musa-Aziz et al., 2009), was localised to the Schwann cell paranode and outer myelin membrane (Fig 3, Fig 3 supplement 1). APQ1 expression also colocalised with Caspr, showing that it was present in the axonal nodal membrane (Einheber et al., 1997). Interestingly, AQP1 was in close proximity to Cx32 in the paranode (M1: 0.400; 0.254, 0.546 and M2: 0.301; 0.199, 0.403). This subcellular localisation of AQP1, would allow it to act as a conduit for CO_2 generated at the axonal node to enter into the Schwann cell paranode and interact with Cx32.

Carbonic anhydrase is present in the paranode

We observed strong expression of CAII in non-myelinated fibres (Fig 4). However, consistent with earlier reports (Cammer and Tansey, 1987) we also observed weaker but more localised expression in myelinated fibres, specifically at the axonal node and Schwann cell paranode (Fig 4).

CO_2-dependent dye loading of Schwann cells in sciatic nerve

We first examined whether Cx32 hemichannels in Schwann cells could be opened by application of hypercapnic aCSF. We exposed isolated sciatic nerves to FITC in aCSF at different levels of PCO_2. As FITC is membrane impermeant but can readily move through channels with large pores such as Cx32 hemichannels (Butler and Dale, 2023), any CO_2-dependent dye loading would thus indicate gating of a CO_2-sensitive large pore channel .

At 35 mmHg, a level of PCO_2 that is too low to open Cx32 hemichannels (Huckstepp et al., 2010; Dospinescu et al., 2019), FITC loading was not observed (Fig 5). However, in the presence of hypercapnic aCSF (70mmHg, sufficient to open Cx32 hemichannels) dye loading into the paranode and outer myelin layers was readily observed (Fig 5, $p < 0.0001$, compared to 35 mmHg). Note that the axons did not load with FITC.

To demonstrate that mitochondrially produced CO_2 could gate Cx32, we used a mitochondrial uncoupler, FCCP, to maximise rates of endogenous CO_2 generation (Balboni and Lehninger, 1986). We found that FCCP caused significantly increased dye loading into Schwann cell paranodes and outer myelin layers ($p < 0.0001$) compared to nerves loaded at 35 mmHg PCO_2 with no FCCP (Fig 5).

CO_2-evoked FITC loading was abolished in the presence of carbenoxolone, indicating FITC entry occurred through a carbenoxolone sensitive hemichannel ($p < 0.0001$, Fig 5). TRPA1 can open with intracellular acidification (Wang et al., 2010), however FITC loading was not blocked by a specific TRPA1 antagonist, HC030031, supporting that dye entry occurred via a connexin rather than TRPA1 ($p = 0.8643$, Fig 5).

Schwann cells express two connexins: Cx32 and Cx31.3 (Jeng et al., 2006; Gerber et al., 2021). Cx31.3 lacks the carbamylation motif and is therefore unlikely to be CO_2 sensitive. To confirm this, we measured ATP release via Cx31.3 expressed in HeLa cells (Liang et al., 2011) in response to changes in PCO_2 and membrane depolarisation, by means of a co-expressed genetically encoded sensor, $GRAB_{ATP}$. HeLa cells transfected only with $GRAB_{ATP}$ but not Cx31.3 did not show any fluorescent changes in response to 70 mmHg PCO_2 or 50 mM K^+ (Fig 5 fig supplement 1). However, in cells transfected with Cx31.3, 50 mM KCl induced ATP release (Fig 5 fig supplement 1). By contrast, a stimulus of 70 mmHg PCO_2 was ineffective at triggering ATP release (Fig 5 fig supplement 1). This confirms that Cx31.3 is not sensitive to CO_2 and makes it most likely that the CO_2-dependent entry of FITC into the Schwann cells was via Cx32.

Activity-dependent loading of FITC into Schwann cells depends on CO_2 production

To test whether Cx32 might open and permit FITC entry into the paranode during action potential propagation, we bathed isolated nerves in aCSF (35 mmHg) and stimulated them electrically at 30 Hz, while measuring the compound action potential (CAP). Upon electrical stimulation, FITC entry into myelin was observed (Fig 6). We confirmed that FITC loaded into paranodes by counterstaining with the paranode marker Caspr (Einheber et al., 1997) (Fig 6). FITC did not load into the axons. FITC loading into myelin was correlated positively with the stimulus duration (Fig 7B).

To test whether this activity dependent FITC loading was also CO_2 dependent, we first manipulated the activity of carbonic anhydrase (CA). Inhibition of CA activity, via acetazolamide, should increase the local PCO_2 as the conversion of CO_2 to carbonic acid will be slowed. We found that acetazolamide (100 μM) greatly increased FITC loading into the

Schwann cell paranode in response 30 Hz stimulation for 1 or 3 minutes (p=0.001 and p=0.0121 respectively, Fig 7A,B).

L-phenylalanine (L-Phe) is an allosteric enhancer of CA activity (Temperini et al., 2006). Myelinating Schwann cells express SLC7A5 (Gerber et al., 2021; Karlsson et al., 2021), the gene that encodes the L-type amino acid transporter. As this transports L-Phe (Nguyen et al., 2021), bath application of L-Phe (1 mM) to isolated nerve, should be effective in enhancing the activity of intracellular CA in Schwann cells. The accelerated conversion of CO_2 to carbonic acid in the presence of L-Phe would be expected to reduce activity dependent dye loading. We indeed observed that treatment with L-Phe greatly reduced activity dependent FITC loading into the Schwann cell paranode (p = 0.0159, Fig 7C,D). Neither acetazolamide nor L-Phe altered the amplitude or the current-amplitude curves of the CAP (Fig 7, fig supplement 1) indicating that these drugs did not affect the excitability of the axon.

As a final test of our hypothesis that activity dependent CO_2 production in the node gates Cx32 in the paranode, we used a specific blocker of AQP1, TC AQP1-1 (80 μM, (Ghosh et al., 2020)). We found blockade of AQP1 greatly reduced FITC loading into the Schwann cell paranode following 5 minutes of stimulation at 30 Hz, compared to that of WT (p< 0.0001, Fig 8). This supports our hypothesis and also indicates that AQP1 is a key conduit for CO_2 to diffuse from the axonal node to the Schwann cell paranode. TC APQ1-1 had no effect on the amplitude or the current-amplitude curves of the CAP (Fig 7, fig supplement 1) indicating that it did not affect the excitability of the axon.

While our data are consistent with activity dependent CO_2 production in the node gating Cx32 in the paranode, they do not eliminate the possible involvement of other signalling pathways such as those mediated by G-protein coupled receptors (GPCRs). We therefore used GDPβS (100 μM) as a general blocker G-protein mediated signalling. As a positive control we showed that application of GDPβS blocked ATP receptor mediated increases in intracellular Ca^{2+} in the paranode (Fig 8, figure supplement 1). However, the application of GDPβS had no effect on activity dependent FITC loading (Fig 8, figure supplement 1).

Enhancement of FITC loading by block of CA is not mediated by pH changes

Inhibition of CA by acetazolamide could plausibly lead to subsequent alkalosis, as the production of HCO_3^- and H^+ ions will be reduced. We therefore tested whether alkalosis by itself was sufficient to enhance activity dependent FITC loading by applying NH_4Cl (100 μM), but this had no effect (p = 0.1257, Fig 8 figure supplement 2).

We quantified the changes in intracellular pH induced upon perfusion of acetazolamide or NH_4Cl by using the pH sensitive dye BCECF (Fig 8 figure supplement 3). We found that NH_4Cl induced greater increases in intracellular pH (change (median; 95% CI): 0.1579; 0.119, 0.1968), than did acetazolamide which had no significant effect on intracellular pH (change: -0.0147; -0.040, 0.011). The enhancement of activity dependent FITC loading by acetazolamide cannot therefore be explained by changes in intracellular pH.

A simplified model of the paranode supports CA as a key regulator of Cx32 gating

To gain further insight, we made a simplified model of the paranode (as a single cell that in effect incorporated the nodal mitochondrion) to explore the effects of CA activity on loading of FITC into Schwann cell paranodes (see Methods and Fig 9). The mitochondrion in this simplified "paranode" was based on a model proposed by Matsuda et al., (2020). The Matsuda model, which accurately replicates the experimentally observed dynamics of ATP production

in mitochondria of myotubes, incorporates the concept of mitochondrial priming: that electrical activity in the myotube enhances the rate of ATP synthesis.

We added a rate of CO_2 production that was proportional to mitochondrial ATP production, endowed the "paranode" with a K^+ channel to give it a resting potential, Cx32 and carbonic anhydrase. The CO_2 sensitive gating of Cx32 was based on the published CO_2 dose response curves (Huckstepp et al., 2010). FITC was assumed to only permeate open Cx32 hemichannels and its transmembrane concentrations were calculated according to the GHK equation assuming that FITC had a net negative charge of -1. CA activity was modelled with Michaelis-Menten kinetics with K_M being based on literature values for CAII. The V_{max} of CA was a free variable that could be altered to mimic the effect of inhibition or allosteric enhancement of CA.

We altered the duration of electrical stimulation of the "paranode" from 1 to 20 mins and calculated the amount of dye loading. With a V_{max} of 15 mM/s, this gave a graph that was very similar to the experimentally obtained data (Fig 9D, compare to Fig 7B). To simulate the effect of acetazolamide we reduced the V_{max} of CA to 1 mM/s, and found an enhancement of dye loading that was once again very similar to the experimentally observed enhancement (Fig 9D, compare to Fig 7B). L-Phe can enhance the activity of CA by up to 3-fold. We found that increasing the V_{max} of CA twofold to 30 mM/s gave a very substantial reduction of dye loading that was similar to the experimentally observed effect of L-Phe (Fig 9D, compare to Fig 7B).

Our simplified model of the paranode suggests that CA is a key regulator of the local PCO_2 and hence Cx32 gating. We also observed that when inhibition of CA was simulated by a reduction of V_{max} to 1 mM/s, the concentration of CO_2 increased to a steady state value of 0.48 mM and there was a steady increase in FITC loading reaching a concentration of 0.7 μM after 30 minutes. Under the "control" conditions CO_2 had a steady state value of 0.05 mM and the FITC concentration after 30 minutes was only 20 pM. There is some support for this prediction of the model as we observed that acetazolamide did indeed increase the background FITC loading of nerve fibres by a small but significant amount (Fig 9, figure supplement 1).

The Matsuda model explicitly incorporates mitochondrial priming by electrical activity, and its use in our model reproduces the experimentally observed dye loading. This suggests that mitochondrial priming might also occur in the node/paranode, although this remains to be tested directly.

Activity dependent entry of Ca^{2+} into the paranode is CO_2 dependent

Our evidence so far supports the hypothesis that Cx32 is gated during action potential propagation by activity dependent generation of CO_2 at the node. During electrical activity Ca^{2+} accumulates in the paranode (Lev-Ram and Ellisman, 1995). As we have previously shown Cx32 to be Ca^{2+} permeable (Butler and Dale, 2023), we tested whether this increase in paranodal Ca^{2+} could be caused by entry via the CO_2-dependent opening of Cx32.

To measure intracellular Ca^{2+} we loaded isolated mouse sciatic nerve with Fluo4-AM. We found that exposure of the nerve to hypercapnic aCSF (70 mmHg) increased Fluo4 fluorescence in paranode-like structures indicating an increase in intracellular Ca^{2+} (Fig 10). The CO_2 evoked increases in Fluo4 fluorescence were blocked by carbenoxolone indicating that they were channel mediated most likely via Cx32 (Fig 10, $p = 0.0087$ CBX compared to control).

Having established the existence of CO_2 dependent Ca^{2+} entry into the paranode, we next determined whether we could observe Ca^{2+} entry into the paranode during electrical stimulation and whether this was also CO_2 dependent. Using Fluo4 loaded sciatic nerves, we

found that we could measure an increase of Ca^{2+} into Schwann cell paranodes during electrical stimulation (Fig 11). Crucially, these transient increases depended upon CO_2 production: they were significantly enhanced by acetazolamide ($p<0.0001$) and reduced by block of AQP1 by TC AQP1-1 ($p<0.0001$) (Fig 12). Thus, the Ca^{2+} entry into the paranode during electrical stimulation depends on CO_2 generated at the node entering the paranode and most likely opening Cx32. This is consistent with earlier reports that show that Ca^{2+} accumulation in the paranode requires extracellular Ca^{2+} (Lev-Ram and Ellisman, 1995).

Activity dependent slowing of conduction velocity is CO_2 dependent

We observed that hypercapnic aCSF, FCCP and electrical activity consistently induced FITC loading into the outer myelin layer, suggesting the occurrence of CO_2 dependent gating of Cx32 in this outermost membrane. Were this to occur, it should increase the leakage of current across the myelin sheath. Saltatory conduction depends on local current circuits travelling down the core of the axon to depolarise that next node (Huxley and Stampfli, 1949). If more current were to leak through the sheath before reaching the next node there should be a small but measurable slowing of conduction velocity (Huxley and Stampfli, 1949; Bakiri et al., 2011). We would therefore predict that during more intense electrical activity in nerve, there should be more CO_2 production and thus a slowing of conduction velocity.

To test this, we measured the CAP firstly under low frequency stimulation (1 Hz), exposed the nerve to a period of high frequency stimulation (15 Hz for 10 mins, to elevate local PCO_2) and then remeasured the CAP under low frequency stimulation (1 Hz). We found high frequency stimulation increased the delay from the stimulus artefact to the peak of the CAP by 0.11 ms (0.04, 0.17) (Fig 13). To demonstrate that this slowing was CO_2-dependent we manipulated the components of the CO_2 signalling system. 100 μM acetazolamide significantly increased the delay to the peak of the CAP caused the high frequency stimulation ($p = 0.0016$, Fig 13). Conversely, 1 mM L-Phe or 80 μM TC AQP1-1 reduced the effect of high frequency stimulation on the delay to the peak of the CAP (respectively $p = 0.0317$ and $p = 0.0079$, Fig 13).

We noticed that the period of high frequency stimulation broadened the CAP and slightly reduced its amplitude. This was particularly exaggerated in the presence of acetazolamide (Fig 13, fig supplement 1). To understand this effect on the shape of the CAP, we made a simple model of the CAP based upon 2000 individual axons each having an identically shaped action potential. To reflect the distribution of fibre diameters reported in sciatic nerve (Assaf et al., 2008) the conduction velocities were given a normal distribution skewed to lower velocities (Fig 13, fig supplement 1). The CAP was simply the sum of all of the individual action potentials. We then slowed the velocity of each fibre by the same proportion and computed the CAP for different amounts of slowing and calculated the 10-90% rise time, the time to peak, and peak amplitude of the CAP (Fig 12, fig supplement 1). This showed that under these simplified assumptions, changes in the shape of the CAP of the type we observed experimentally would be expected from slowing the conduction velocities in all fibres by the same proportion.

Discussion

Activity dependent gating of Cx32

In this paper we have investigated the mechanism of activity dependent Cx32 hemichannel gating in peripheral myelin. Previously, the opening of Cx32 has been posited to depend on either its intrinsic voltage sensitivity (Abrams et al., 2002) or as a downstream consequence of an increase in cytosolic Ca^{2+} within the paranode (Stauch et al., 2012; Carrer et al., 2018). Here,

we have tested an alternative hypothesis: that cell-to-cell signalling mediated via CO_2 produced in the axonal node is the primary trigger for Cx32 gating in the paranode. Our hypothesis explicitly links Cx32 opening in the paranode to the energetic demands of action potential propagation in the node.

In our experiments, we assessed Cx32 gating via entry of the membrane impermeant dye, FITC. Our results support our new hypothesis in several respects. Firstly, Cx32 gating in response to axon stimulation was greatly reduced by blocking AQP1, which is CO_2 permeable (Endeward et al., 2006; Musa-Aziz et al., 2009; Michenkova et al., 2021) and thus provides a route for passage of CO_2 from node to paranode. Secondly, inhibition of CA with acetazolamide greatly increased the activity dependent gating of Cx32. Thirdly, facilitation of CA activity by applying an allosteric enhancer, L-Phe, greatly reduced activity dependent gating of Cx32. Fourthly, the effect of FCCP showed that mitochondrially generated CO_2 was sufficient to gate Cx32. Finally, application of GDPβS to block all GPCR based signalling had no effect on activity-dependent gating of Cx32. Together these results suggest that CO_2 is acting as a cell-to-cell signal and is the prime trigger for Cx32 opening during action potential propagation. In the light of these results, it is interesting that elasmobranchs, the first vertebrates to evolve a fully myelinated nervous system, have an orthologue of Cx32 that has identical CO_2 sensitivity to human Cx32 (Dospinescu et al., 2019).

As there are no selective pharmacological blockers for Cx32, our evidence that Cx32 is the conduit for activity and CO_2 dependent FITC loading into the paranode is indirect. Nevertheless, our combined evidence is compelling for the following reasons. Cx32 is the only known large-pored channel expressed in Schwann cells that is directly sensitive to gaseous CO_2. We know that FITC permeates Cx32 and the CO_2 dose dependence of FITC loading matches that of Cx32. We have eliminated both Cx31.3 (not CO_2 sensitive) and TRPA1 (unaffected by a selective blocker of this channel) as the conduit. By contrast, dye entry is blocked by carbenoxolone a non-specific connexin hemichannel blocker and the entry of FITC into the Schwann cell but not the axon matches the cellular localisation of Cx32 (present in paranode and outer myelin layer).

The important roles of AQP1 and carbonic anhydrase

Our physiological evidence for CO_2 as a signal between the node and paranode is supported by the cellular localisation of the critical components required for this signalling. Mitochondria, the source of CO_2, are located at the node. AQP1 is expressed in both the nodal and paranodal membranes. This is important as the binding site for CO_2 on Cx32 is intracellular and CO_2 must therefore cross both the nodal and paranodal membranes. Cx32 is expressed in the paranode and colocalises with AQP1. CA, which provides an efficient removal mechanism for CO_2, is also located at the paranode.

Whilst there has been controversy over the role of CO_2 permeable channels in enabling transmembrane CO_2 fluxes, it is now accepted that biological membranes are only poorly permeable to CO_2 and a channel mediated mechanism is required (Boron et al., 2011). Our data further support this idea, as blockade of APQ1 prevents the activity dependent gating of Cx32. Given that our data also show that CA activity limits the gating of Cx32, the colocalization of AQP1 and Cx32 may be important. As AQP1 will be the entry point for CO_2 into the paranode, its colocalization with Cx32 may favour CO_2 binding to Cx32 over capture and conversion to carbonic acid by CA.

Our simplified model of the paranode sheds further light on the regulation of CO_2 signalling and the gating of Cx32. The Matsuda model (Matsuda et al., 2020) incorporates priming of mitochondrial ATP production by electrical activity and hence this is also implicit in our paranode model. Mitochondrial priming will make CO_2 production more rapid than if it depended on ATP depletion to occur first. This implies that CO_2 production could vary relatively quickly with activity patterns and thus report the dynamics of action potential firing. It will be important to directly test this prediction by measuring the dynamics of mitochondrial ATP production in the node relative to imposed electrical activity.

Our model also predicts that complete inhibition of CA will give some Cx32 gating under non-stimulated conditions. We observed increased baseline loading of FITC into the nerves during acetazolamide giving support for this prediction. This suggests that an important role of CA is to prevent basal rates of CO_2 production being sufficient to gate Cx32. Our model also suggests that CA activity regulates the extent to which activity dependent production of CO_2 can gate Cx32. The effects of L-Phe and acetazolamide lend support to this prediction. Thus, the model suggests that CA regulates the dynamic range of the CO_2 signal and is likely to be an important regulator of CO_2 mediated signalling.

Physiological consequences of CO_2 dependent signalling

We have further shown that two other aspects of Schwann cell physiology and function depend on the CO_2-dependent gating of Cx32. Firstly, the well documented increase of intracellular Ca^{2+} into the paranode evoked by nerve stimulation appears to largely depend on the opening of Cx32 and can be modified in the same way as dye loading by manipulating CA activity or blocking AQP1. Secondly, given the localisation of Cx32 in the outer myelin layer and the observation of activity- and CO_2-dependent dye loading into that outer layer, we hypothesised that there should be activity dependent slowing of nerve conduction. This is because any opening of Cx32 hemichannels should reduce the resistance to current flow across the myelin sheath. We did indeed observe a small degree of activity dependent slowing of nerve conduction velocity. Crucially, this too depended upon CO_2 production and could be altered by manipulating CA activity or blocking AQP1.

Links to CMTX

Given our evidence suggests that the CO_2 sensitivity of Cx32 is critical for its gating during action potential propagation, we might expect that any mutations that affect this sensitivity could precipitate CMTX. We have previously examined the effect of 14 CMTX mutations on the CO_2 sensitivity of Cx32 (Butler and Dale, 2023). We found that 5 completely removed its CO_2 sensitivity, 3 greatly reduced its sensitivity while the remainder had no apparent effect. It should be noted that two mutations of K124 (Bone et al., 1997; Fattahi et al., 2017) and K104 (Williams et al., 1999; Wang et al., 2015), the critical residues for detection of CO_2 (K104E, K104T, K124E and K124N, not included in our published study), have also been identified as possible CMTX mutations.

These results, while supportive of our hypothesis, are not conclusive as several of the 8 CMTX mutations that altered CO_2 sensitivity have been documented to also affect other facets of channel function. However, the CMTX mutation E102G stands out as causing moderate severity CMTX while still permitting the formation of gap junction channels and hemichannels with apparently normal voltage dependence and ATP permeability. Because E102G involves the loss of CO_2 sensitivity of the hemichannel in the absence of other known functional effects on the hemichannel (Abrams et al., 2003) it lends some support to the hypothesis that the CO_2-

dependence of Cx32 may be important for the health of myelin and that its loss could precipitate CMTX. Further exploration of CO_2- and Cx32-dependent signalling in myelin may suggest new strategies to treat peripheral neuropathies and peripheral nerve injury,

Methods

All experiments were performed in accordance the United Kingdom Home Office Animals (Scientific Procedures) Act (1986) with project approval from the University of Warwick's AWERB.

Sciatic nerve isolation

All mice used were C57BL/6, aged at least 6 weeks. Sciatic nerves were isolated following the protocol described in Rich et al., 2018. Placing a few drops of ice cold aCSF loosened the perineural membrane allowing its easy removal with forceps, beginning at one cut end of the nerve, and moving inward. Once the perineural membrane was removed, forceps were carefully placed in between the seams of the larger bundle of fibres before being teased apart with careful lateral movement. Removal of the perineural membrane and slight teasing was sufficient to obtain dye loading, with extensive dissection to small bundles or individual fibres only occurring post- fixation for immunohistochemistry and visualisation.

Immunocytochemistry

Antibodies used:

Antibody	Supplier	ID	RRID	Dilution	Reference
KCNQ2 (Kv7.2)	Abcam	ab22897	AB_775890	1/500	(Kapell et al., 2023)
KCNA2 (Kv1.2)	Sigma Aldrich	MABN77	AB_10806493	1/500	(Otani et al., 2020)
Caspr	Sigma Aldrich	MABN69	AB_10806491	1/250	(Sanchez-de la Torre et al., 2022)
Connexin 32	ThermoFisher	13-8200	AB_2533037	1/250	(Fowler et al., 2013)
Aquaporin-1	Bioorbit	orb10122	AB_10751997	1/250	(Pelagalli et al., 2018)
Sideroflexin-1	Proteintech	12296-1-AP	AB_2185814	1/1000	(Fowler et al., 2013)
Cytochrome C	Invitrogen	54205-RBM6-P0	AB_3678654	1/500	Validated by supplier
Carbonic Anhydrase 2	Invitrogen	PA5-78897	AB_2746013	1/500	(Zigo et al., 2022)

Sciatic nerves were first washed with PBS three times, before being fixed in 4% PFA for 45 mins. Nerves were then washed in PBS three times and blocked using PBS containing 4% BSA and 0.1% Triton X-100 for 24 hr. Nerves were teased prior to immunostaining. Primary antibody was diluted in PBS containing 4% BSA and 0.1% Triton X-100 and added to nerves and left to incubate, constantly shaking, for 48hrs at 4°C. Nerves were then washed using PBS containing 0.1% Triton X-100 six times at 10 min intervals. The appropriate secondary antibodies diluted in PBS containing 4% BSA and 0.1% Triton X- 100 and added to coverslips and left to incubate, constantly moving, for 2.5 h. The secondary antibody was washed using PBS containing 0.1% Triton X-100 six times at 10 min intervals. Nerves were again blocked for 24hrs. To co-stain with a further primary antibody from the same species, antibody conjugation was used (ProteinTech FlexAble corallite®). Conjugated antibodies were diluted in PBS containing 4% BSA and 0.1%

Triton X-100 and added to nerves and left to incubate, constantly moving, for 48 hr at 4°C. The conjugated antibody was washed using PBS containing 0.1% Triton X-100 six times at 10 min intervals. Nerves were then placed onto a glass slide and further dissected using the tips of hypodermic syringes, yielding individual nerve fibres. Nerves where then mounted using Fluorshield™ with DAPI mounting medium (Sigma-Aldrich, Cat# F6057), placing a glass coverslip on top. Nerve fibres were subsequently imaged using the Zeiss-880 and Zeiss 980 confocal LSMs, specifically using the 488, 561 and 630 nm lasers. FIJI software was used for further analysis. Images were taken on a Nikon N-SIM S with dual camera, utilising a 100X oil immersion lens. 470, 561 and 640 nm lasers were used.

Solutions used

Control (35 mmHg PCO_2) aCSF: 124 mM NaCl, 3 mM KCl, 2 mM $CaCl_2$, 26 mM $NaHCO_3$, 1.25 mM NaH_2PO_4, 1 mM $MgSO_4$, 10 mM D-glucose saturated with 95% O_2/5% CO_2, pH 7.4.

Hypercapnic (70 mmHg) aCSF: 73 mM NaCl, 3 mM KCl, 2 mM $CaCl_2$, 80 mM $NaHCO_3$, 1.25 mM NaH_2PO_4, 1 mM $MgSO_4$, 10 mM D-glucose, saturated with ~12% CO_2 (with the balance being O_2) to give a pH of 7.4.

Depolarising (35 mmHg PCO_2) aCSF: 77 mM NaCl, 50 mM KCl, 2 mM $CaCl_2$, 26 mM $NaHCO_3$, 1.25 mM NaH_2PO_4, 1 mM $MgSO_4$, 10 mM D-glucose saturated with 95% O_2/5% CO_2, pH 7.4.

Pharmacological agents

Compound	**Supplier**	**Concentration (μM)**
Acetazolamide	Sigma Aldrich A6011	100
Ammonium chloride	Invitrogen A15000.0B	100
GDPβS	Sigma Aldrich G7637	100
L-Phenylalanine	Sigma Aldrich P2126	1000
TC AQP1-1	Tocris 5412	80

Dye loading assay

Isolated nerves were obtained as described above and slightly teased apart with sharp needles as this was found to produce more profound and reliable dye-loading.

CO_2-dependent dye loading

Isolated sciatic nerves were first washed in control aCSF before being superfused with either 35 mmHg aCSF or 70 mmHg aCSF containing 50 μM fluorescein isothiocyanate (FITC) for 10 minutes. To induce endogenous CO_2 production via mitochondrial uncoupling isolated nerves were superfused with 35mmHg aCSF containing 10 μM FCCP (APExBIO) for 10 minutes. Following this, FITC was washed off by superfusion with 35 mmHg aCSF with no dye for 10 minutes. The nerves were then transferred through a series of vessels with 35mmHg aCSF to remove any remaining FITC.

Dye loading triggered by electrical stimulation

Nerves were pre-incubated in 35 mmHg aCSF, and any desired pharmacological agent, for 10 minutes prior to recording. Polished glass suction electrodes wrapped with a silver wire and

backfilled with aCSF were used for stimulation and recording. The ends of nerves were gently sucked up into the suction electrodes such that orthodromic recordings were made, described in (Rich et al., 2018).

The recordings of the stimulus evoked CAPs were controlled by a National Instruments A/D interface (Model PCIe 6321) using the Strathclyde electrophysiology software program, WinWCP. A stimulator, Digitimer model DS3, was used to stimulate the nerve. The signal was amplified x1000 by an A-M Systems Inc Model 3000 AC/DC differential amplifier (A-M Systems, Sequim, WA 98382, USA). The signal was filtered at 20 kHz and 1 Hz and acquired at 20 kHz. To assess the validity of the CAP, the nerve was crushed between forceps at the conclusion of the experiment, leaving only the transient artefact.

Once a recording of the CAP had been successfully established, nerves were exposed to FITC during electrical stimulation at (30 Hz) of different durations (1-10 minutes). They were then washed to remove FITC as described above. As each mouse possesses 2 sciatic nerves, when pharmacological agents were used, one nerve from each animal would be stimulated in the absence of any pharmacological agents as a matched control. I-V curves were recorded prior to drug pre-incubation, during pre-incubation and following stimulation, to assess any effects of the used compound on the CAP. From the CAP traces rise time, rate of rise and latency could be calculated using WinWCP.

Fixation and imaging of dye-loaded nerves

Nerves were then fixed using 4% PFA for 45 minutes. Nerves were subsequently imaged using Zeiss 880 or 980 confocal LSMs, specifically using the 488, 561 and 633nm lasers. FIJI software was used for further analysis. The statistical replicate was a single region of interest (ROI) and these were obtained from 5 nerves for each condition.

Measurement of intracellular pH with BCECF

Mouse sciatic nerve was dissected as previously described. BCECF-AM dissolved in DMSO was diluted into 35 mmHg aCSF to a final concentration of 2.5 μM. A hypodermic needle was blunted and joined to a fine glass capillary via a short length of tubing. Etched tungsten wire was used to make a small incision in the middle on the nerve, from which the nerve was teased open slightly. Whilst holding the incision open the capillary loaded with BCECF was inserted and injected. The nerve was placed into 35mmHg aCSF to wash for 3 minutes. The nerve was then placed into a recording chamber, immobilised with a platinum wire harp and superfused with 35 mmHg aCSF. The BCECF-loaded nerves were imaged by epifluorescence (Scientifica Slice Scope, Cairn Research OptoLED illumination, 60x water Olympus immersion objective, NA 1.0, Hamamatsu ImagEM EM-SSC camera, Metafluor software). BCECF was excited using 470nm LED, with fluorescent emission being recorded every 4 seconds between 507 and 543nm. Once a stable fluorescence baseline was reached, the various test solutions were superfused onto the nerve. Intracellular pH was then calibrated using Nigericin (James-Kracke, 1992).

The statistical replicate was a single nerve and 5 nerves were recorded for each condition.

Measurement of intracellular Ca^{2+} with Fluo4

Fluo4-AM dissolved in Pluronic™ F-127 (Thermo Fisher Scientific P3000MP) with constant sonication and vortexing and was diluted into 35mmHg aCSF to a final concentration of 2.5 μM. Nerves were then incubated for 20 minutes before being washed in 35 mmHg aCSF.

Nerves were placed into the recording chamber and anchored with a platinum harp. The nerve was perfused with 35 mmHg aCSF until a stable baseline was reached. The desired solution was then perfused until a stable level had been reached before being washed.

To enable simultaneous electrical stimulation and Fluo4 imaging, the nerves were mounted between electrodes within a bespoke micro-perfusion chamber constructed of Sylgard™-184. Proprietary software was used to control nerve stimulation at 15Hz, record the CAP and perform offline analysis.

Nerves were imaged by epifluorescence (Scientifica Slice Scope, Cairn Research OptoLED illumination, 60x water Olympus immersion objective, NA 1.0, Hamamatsu ImagEM EM-SSC camera, Metafluor software). Fluo4 was excited with a 470nm LED, and fluorescent emission between 507 and 543nm recorded every 4 seconds.

The statistical replicate was a single ROI (paranode) and these were obtained from 5 nerves for each condition.

Measurement of activity dependent conduction velocity slowing

Using isolated nerves, CAPs were recorded as described above using the Strathclyde electrophysiology software. The baseline of CAP was recorded at low frequency (1Hz) for 30 seconds. High frequency stimulation (30 Hz) was applied for 10 minutes. Following this the nerves were then stimulated for 30 seconds at 1Hz. The CAPs from before and after high frequency stimulation were averaged and compared. A recording from an isolated nerve was considered as a statistical replicate.

Cell culture and transfection

The Cx31.3 gene sequence were synthesized by IDT and subcloned into the pCAG-GS-mCherry vector. DNA gBlock was amplified using PCR with primers (IDT) Plasmids were generated using Gibson assembly. The presence of the correct assembly was confirmed by DNA sequencing (GATC biotech). The Cx31.3 construct was inserted upstream of mCherry, with a short 12 amino acid linker (GVPRARDPPVAT).

pDisplay-GRAB_ATP1.0-IRES-mCherry-CAAX was a gift from Yulong Li (Addgene plasmid # 167582 ; http://n2t.net/addgene:167582 ; RRID:Addgene_167582)

Parental HeLa DH cells were grown in Low-glucose Dulbecco's modified eagle medium (DMEM) supplemented with 10% FBS and 50µg/mL penicillin/streptomycin. The HeLa DH cells were plated onto coverslips at a density of 7.5 X 10^4 cells per well of a 6 well plate and transiently transfected using a mixture of 1 µg each of the Cx31.3 construct and $GRAB_{ATP}$ and 3 µg PEI for 6hrs. Cells were imaged 48 hours after transfection. We used a protocol to measure ATP release from cells developed and described in our previous work (Butler and Dale, 2023).

Analysis of $GRAB_{ATP}$ fluorescence

Analysis of $GRAB_{ATP}$ was performed in ImageJ (Schneider et al., 2012). Cell recordings were corrected for any motion using the Image Stabilizer plugin (Li, 2008). For cells expressing both Cx31.3 and $GRAB_{ATP}$, an ROI was drawn around the $GRAB_{ATP}$ expression and median fluorescence measured for each image. The fluorescence pixel intensity (F) was normalised to the baseline fluorescence (F_0). The change in normalised fluorescence ($\Delta F/F_0$) evoked each stimulus, CO_2 and 50 mM KCl, was recorded for each cell.

We converted changes in normalised fluorescence evoked by 70 mmHg pCO_2 and 50 mM KCl into the concentration of ATP released by normalising them to the $\Delta F/F_0$ produced by a 3 μM ATP calibration solution. Statistical comparisons were performed considering each cell as an independent replicate. Five transfections were performed.

Analysis of Immunohistochemical colocalization

The JACOP plugin (Bolte and Cordelieres, 2006) was used to calculate the Manders' coefficients M1 and M2. The convention we have used throughout the paper is that for colocalization of A with B, M1 represents the proportion of A pixels that overlap with B pixels, and M2 would represent the proportion of B pixels overlapping with A pixels.

As a control, one channel was rotated 90^0 and analysis was re-run using the same thresholds. Each datapoint represents an ROI, or a paranode, with all data points coming from at least 5 nerves.

Modelling of paranode

The paranode was modelled as a cell with a mitochondrion, a K^+ leak channel, Cx32 and CA. Mitochondrial ATP production was modelled as per Matsuda et al (Matsuda et al., 2020). This involves a time-dependent variable Y, that stimulates ATP production, where X is a variable that is proportional to the duration of electrical stimulation, Y_0 is the steady state value of Y and relaxes to that value with a time constant of τ_1. K_{d1} and n_1 are parameters for the Hill equation that determines how variable X alters the value of Y:

1. $$\frac{dY}{dt} = \frac{X^{n_1}}{K_{d_1}+X^{n_1}} - \frac{Y-Y_0}{\tau_1}$$

A time-dependent variable Z determines the use of ATP:

2. $$\frac{dZ}{dt} = \frac{X^{n_2}}{K_{d_2}+X^{n_2}} - \frac{Z-Z_0}{\tau_2}$$

where Z_0 is the steady state value of Z and relaxes to that value with a time constant of τ_2 and K_{d2} and n_2 are parameters for the Hill equation that determine how variable X alters the value of Z.

The rate of change of ATP concentration is thus:

3. $$\frac{dATP}{dt} = k_1.Y - k_2.Z.ATP$$

Where k_1 and k_2 are rate constants for synthesis and breakdown of ATP respectively.

To adapt this model to the paranode we first defined the rate of CO_2 production is proportional to ATP production, and used the Michaelis Menten equation to calculate CO_2 conversion to carbonic acid:

4. $$\frac{dCO_2}{dt} = \alpha.k_1.Y - \frac{V_{max}.CO_2}{CO_2+K_m} - k_s.CO_2$$

Where V_{max} and K_m are the maximal velocity of CA and affinity of CA for CO_2 respectively, α is a rate constant for the production of CO_2. For completeness, we also allowed for spontaneous conversion of CO_2 to carbonic acid -determined by the first order rate constant, k_s. Variables Y and k_1 have the same meaning as in equation 3.

The rate of membrane potential change of the paranode was calculated from:

5. $\frac{dV}{dt} = -C_m.(I_K + I_{Cx32} + I_{FITC})$

Where C_m is the whole cell membrane capacitance, I_K the K^+ leak current, I_{Cx32} the current through Cx32 and I_{FITC} the current carried by FITC.

I_K is described by the Goldman Hodgkin Katz (GHK) equation:

6. $I_K = P_K.\frac{z^2VF^2}{RT}.\frac{K_i - K_o.e^{-zVF/RT}}{1-e^{-zVF/RT}}$

Where P_K is the maximal whole cell permeability to K^+, z the valence. R is the universal gas constant, T the absolute temperature (in Kelvin) and F the Faraday constant. K_i and K_o are respectively the intracellular and extracellular concentrations of K^+.

I_{Cx32} is described by:

7. $I_{Cx32} = G_{Cx32}.\frac{{CO_2}^H}{{CO_2}^H + K_{Cx32}}.(V - V_{rev})$

Where G_{Cx32} is the maximal whole cell conductance for Cx32, K_{Cx32} is the affinity of Cx32 for CO_2, H is the Hill coefficient of CO_2 binding and V_{rev} is the reversal potential of the current through Cx32.

I_{FITC} (through Cx32) is described by:

8. $I_{FITC} = P_{Cx32}.\frac{{CO_2}^H}{{CO_2}^H + K_{Cx32}}.\frac{z^2VF^2}{RT}.\frac{FITC_i - FITC_o.e^{-zVF/RT}}{1-e^{-zVF/RT}}$

Where P_{Cx32} is the maximal whole cell permeability of Cx32 to FITC and z the valence of FITC. R is the universal gas constant, T the absolute temperature (in Kelvin) and F the Faraday constant. $FITC_i$ and $FITC_o$ are respectively the intracellular and extracellular concentrations of FITC. K_{Cx32} and H have the same meaning as in equation 7.

The rate of change of $FITC_i$ with time is thus:

9. $\frac{dFITC_i}{dt} = \frac{I_{FITC}}{F}$

Where F is the Faraday constant.

These differential equations were coded with Matlab, and a 4th order Runge-Kutta ODE solver with adaptive step size used to numerically integrate them and thus calculate the production of CO_2 during electrical stimulation and the extent FITC loading. The Matlab code along with a command line interface is presented in the source files: CO2Cx32Plot.m and CO2Cx32Model.m.

Modelling of CAP

Using Matlab, a compound action potential was computed from summing 2000 individual action potentials based on the product of two Boltzmann equations to give a realistic shape (compoundAP.m). The action potentials were given a random delay (representing conduction velocity) based on a mean ± SD described by a Gaussian distribution with a skew factor. This was chosen to reflect the skewed distribution of axon diameters in the sciatic nerve (Assaf et al., 2008). Slowing could be introduced by slowing the conduction velocity of every individual action potential by a fixed proportion of its delay.

Statistical analysis

All quantitative data are presented as box and whisker plots where the box represents the interquartile range, the bar represents the median, and the whiskers represent 1.5 times the interquartile range, or the range if this is less. Individual data points are superimposed onto boxplots. Statistical analysis was via the Kruskal Wallis one-way ANOVA (KW test) followed by pairwise Mann Whitney U-tests with correction for multiple comparisons via the false discovery method (Curran-Everett, 2000) with the maximum rate of false discovery set at 0.05. For analysis of the $GRAB_{ATP}$ recordings in which the CO_2 and 50 mM KCl stimuli were applied to the same cell, these data were considered to be paired and comparisons of the amount of ATP released by each stimulus was therefore performed with the Wilcoxon Matched Pairs Signed Rank test. All pairwise tests were two sided and all calculations performed with GraphPad PRISM.

Acknowledgements

We thank Dr Joao Correia, Institute of Microbiology & Infection, University of Birmingham, for assistance with the super resolution microscopy.

Author Contributions: JB: Conceptualisation, data collection and curation, investigation, writing – original draft, formal analysis. LM: Investigation, data collection and curation. AB: Conceptualisation, training and review. ND: Conceptualisation, modelling, supervision, writing – original draft, review and editing. All authors reviewed the final draft.

Funding: JB was supported by the Biotechnology and Biological Sciences Research Council (BBSRC) and University of Warwick funded Midlands Integrative Biosciences Training Partnership (MIBTP) grant number BB/T00746X/1.

Conflicts of interest: The authors declare that there are no conflicts of interest.

Data availability: All data is included in the supplementary files for each figure.

References

Abrams CK, Bennett MV, Verselis VK, Bargiello TA (2002) Voltage opens unopposed gap junction hemichannels formed by a connexin 32 mutant associated with X-linked Charcot-Marie-Tooth disease. Proc Natl Acad Sci U S A 99:3980-3984.

Abrams CK, Freidin M, Bukauskas F, Dobrenis K, Bargiello TA, Verselis VK, Bennett MV, Chen L, Sahenk Z (2003) Pathogenesis of X-linked Charcot-Marie-Tooth disease: differential effects of two mutations in connexin 32. J Neurosci 23:10548-10558.

Assaf Y, Blumenfeld-Katzir T, Yovel Y, Basser PJ (2008) AxCaliber: a method for measuring axon diameter distribution from diffusion MRI. Magn Reson Med 59:1347-1354.

Bakiri Y, Karadottir R, Cossell L, Attwell D (2011) Morphological and electrical properties of oligodendrocytes in the white matter of the corpus callosum and cerebellum. J Physiol 589:559-573.

Balboni E, Lehninger AL (1986) Entry and exit pathways of CO2 in rat liver mitochondria respiring in a bicarbonate buffer system. J Biol Chem 261:3563-3570.

Balice-Gordon RJ, Bone LJ, Scherer SS (1998) Functional gap junctions in the schwann cell myelin sheath. J Cell Biol 142:1095-1104.

Bergoffen J, Scherer SS, Wang S, Scott MO, Bone LJ, Paul DL, Chen K, Lensch MW, Chance PF, Fischbeck KH (1993) Connexin mutations in X-linked Charcot-Marie-Tooth disease. Science 262:2039-2042.

Bolte S, Cordelieres FP (2006) A guided tour into subcellular colocalization analysis in light microscopy. Journal of microscopy 224:213-232.

Bone LJ, Deschenes SM, Balice-Gordon RJ, Fischbeck KH, Scherer SS (1997) Connexin32 and X-linked Charcot-Marie-Tooth disease. Neurobiol Dis 4:221-230.

Boron WF, Endeward V, Gros G, Musa-Aziz R, Pohl P (2011) Intrinsic CO2 permeability of cell membranes and potential biological relevance of CO2 channels. Chemphyschem 12:1017-1019.

Bortolozzi M (2018) What's the Function of Connexin 32 in the Peripheral Nervous System? Frontiers in molecular neuroscience 11:227.

Brotherton DH, Savva CG, Ragan TJ, Dale N, Cameron AD (2022) Conformational changes and CO2-induced channel gating in connexin26. Structure 30:697-706.

Brotherton DH, Nijjar S, Savva CG, Dale N, Cameron AD (2024) Structures of wild-type and a constitutively closed mutant of connexin26 shed light on channel regulation by CO2. eLife 13:RP93686.

Butler J, Dale N (2023) X-linked Charcot Marie Tooth mutations alter CO(2) sensitivity of connexin32 hemichannels. Front Cell Neurosci 17:1330983.

Cammer W, Tansey FA (1987) Immunocytochemical localization of carbonic anhydrase in myelinated fibers in peripheral nerves of rat and mouse. J Histochem Cytochem 35:865-870.

Carrer A, Leparulo A, Crispino G, Ciubotaru CD, Marin O, Zonta F, Bortolozzi M (2018) Cx32 hemichannel opening by cytosolic Ca2+ is inhibited by the R220X mutation that causes Charcot-Marie-Tooth disease. Hum Mol Genet 27:80-94.

Curran-Everett D (2000) Multiple comparisons: philosophies and illustrations. Am J Physiol Regul Integr Comp Physiol 279:R1-8.

Dospinescu V-M, Nijjar S, Spanos F, Cook J, de Wolf E, Biscotti MA, Gerdol M, Dale N (2019) Structural determinants of CO2-sensitivity in the β connexin family suggested by evolutionary analysis. Communications Biology 2:331.

Einheber S, Zanazzi G, Ching W, Scherer S, Milner TA, Peles E, Salzer JL (1997) The axonal membrane protein Caspr, a homologue of neurexin IV, is a component of the septate-like paranodal junctions that assemble during myelination. J Cell Biol 139:1495-1506.

Endeward V, Musa-Aziz R, Cooper GJ, Chen LM, Pelletier MF, Virkki LV, Supuran CT, King LS, Boron WF, Gros G (2006) Evidence that aquaporin 1 is a major pathway for CO2 transport across the human erythrocyte membrane. Faseb j 20:1974-1981.

Fairweather N, Bell C, Cochrane S, Chelly J, Wang S, Mostacciuolo ML, Monaco AP, Haites NE (1994) Mutations in the connexin 32 gene in X-linked dominant Charcot-Marie-Tooth disease (CMTX1). Hum Mol Genet 3:29-34.

Fattahi Z, Kalhor Z, Fadaee M, Vazehan R, Parsimehr E, Abolhassani A, Beheshtian M, Zamani G, Nafissi S, Nilipour Y, Akbari MR, Kahrizi K, Kariminejad A, Najmabadi H (2017) Improved diagnostic yield of neuromuscular disorders applying clinical exome sequencing in patients arising from a consanguineous population. Clin Genet 91:386-402.

Fowler SL, Akins M, Zhou H, Figeys D, Bennett SA (2013) The liver connexin32 interactome is a novel plasma membrane-mitochondrial signaling nexus. Journal of proteome research 12:2597-2610.

Gao H, He C, Fang X, Hou X, Feng X, Yang H, Zhao X, Ma T (2006) Localization of aquaporin-1 water channel in glial cells of the human peripheral nervous system. Glia 53:783-787.

Gerber D, Pereira JA, Gerber J, Tan G, Dimitrieva S, Yanguez E, Suter U (2021) Transcriptional profiling of mouse peripheral nerves to the single-cell level to build a sciatic nerve ATlas (SNAT). eLife 10.

Ghosh S, Verma A, Kumar V, Pradhan D, Selvapandiyan A, Salotra P, Singh R (2020) Genomic and Transcriptomic Analysis for Identification of Genes and Interlinked Pathways Mediating Artemisinin Resistance in Leishmania donovani. Genes (Basel) 11.

Hattori N, Yamamoto M, Yoshihara T, Koike H, Nakagawa M, Yoshikawa H, Ohnishi A, Hayasaka K, Onodera O, Baba M, Yasuda H, Saito T, Nakashima K, Kira J, Kaji R, Oka N, Sobue G (2003) Demyelinating and axonal features of Charcot-Marie-Tooth disease with mutations of myelin-

related proteins (PMP22, MPZ and Cx32): a clinicopathological study of 205 Japanese patients. Brain 126:134-151.
Huckstepp RT, Eason R, Sachdev A, Dale N (2010) CO2-dependent opening of connexin 26 and related beta connexins. J Physiol 588:3921-3931.
Huxley AF, Stampfli R (1949) Evidence for saltatory conduction in peripheral myelinated nerve fibres. J Physiol 108:315-339.
James-Kracke MR (1992) Quick and accurate method to convert BCECF fluorescence to pHi: calibration in three different types of cell preparations. J Cell Physiol 151:596-603.
Jeng LJ, Balice-Gordon RJ, Messing A, Fischbeck KH, Scherer SS (2006) The effects of a dominant connexin32 mutant in myelinating Schwann cells. Mol Cell Neurosci 32:283-298.
Kapell H et al. (2023) Neuron-oligodendrocyte potassium shuttling at nodes of Ranvier protects against inflammatory demyelination. The Journal of clinical investigation 133.
Karlsson M et al. (2021) A single-cell type transcriptomics map of human tissues. Sci Adv 7.
Lev-Ram V, Ellisman MH (1995) Axonal activation-induced calcium transients in myelinating Schwann cells, sources, and mechanisms. J Neurosci 15:2628-2637.
Li K (2008) The image stabilizer plugin for ImageJ. In.
Liang WG, Su CC, Nian JH, Chiang AS, Li SY, Yang JJ (2011) Human connexin30.2/31.3 (GJC3) does not form functional gap junction channels but causes enhanced ATP release in HeLa cells. Cell Biochem Biophys 61:189-197.
Matsuda N, Hironaka K-i, Fujii M, Wada T, Kunida K, Inoue H, Eto M, Hoshino D, Furuichi Y, Manabe Y, Fujii NL, Noji H, Imamura H, Kuroda S (2020) Monitoring and mathematical modeling of mitochondrial ATP in myotubes at single-cell level reveals two distinct population with different kinetics. Quantitative Biology 8:228-237.
Meier C, Dermietzel R, Davidson KGV, Yasumura T, Rash JE (2004) Connexin32-Containing Gap Junctions in Schwann Cells at the Internodal Zone of Partial Myelin Compaction and in Schmidt–Lanterman Incisures. The Journal of Neuroscience 24:3186.
Meigh L, Greenhalgh SA, Rodgers TL, Cann MJ, Roper DI, Dale N (2013) CO2 directly modulates connexin 26 by formation of carbamate bridges between subunits. eLife 2:e01213.
Michenkova M, Taki S, Blosser MC, Hwang HJ, Kowatz T, Moss FJ, Occhipinti R, Qin X, Sen S, Shinn E, Wang D, Zeise BS, Zhao P, Malmstadt N, Vahedi-Faridi A, Tajkhorshid E, Boron WF (2021) Carbon dioxide transport across membranes. Interface Focus 11:20200090.
Murakami T, Garcia CA, Reiter LT, Lupski JR (1996) Charcot-Marie-Tooth disease and related inherited neuropathies. Medicine 75:233-250.
Musa-Aziz R, Chen LM, Pelletier MF, Boron WF (2009) Relative CO2/NH3 selectivities of AQP1, AQP4, AQP5, AmtB, and RhAG. Proc Natl Acad Sci U S A 106:5406-5411.
Nguyen YTK, Ha HTT, Nguyen TH, Nguyen LN (2021) The role of SLC transporters for brain health and disease. Cell Mol Life Sci 79:20.
Nijjar S, Brotherton DH, Butler J, Dospinescu V-M, Gannon H, Linthwaite VL, Cann MJ, Cameron A, Dale N (2025) Multiple carbamylation events are required for differential modulation of Cx26 hemichannels and gap junctions by CO_2. The Journal of physiology.
Nualart-Marti A, del Molino EM, Grandes X, Bahima L, Martin-Satue M, Puchal R, Fasciani I, Gonzalez-Nieto D, Ziganshin B, Llobet A, Barrio LC, Solsona C (2013) Role of connexin 32 hemichannels in the release of ATP from peripheral nerves. Glia 61:1976-1989.
Ohno N, Kidd GJ, Mahad D, Kiryu-Seo S, Avishai A, Komuro H, Trapp BD (2011) Myelination and axonal electrical activity modulate the distribution and motility of mitochondria at CNS nodes of Ranvier. J Neurosci 31:7249-7258.
Otani Y, Ohno N, Cui J, Yamaguchi Y, Baba H (2020) Upregulation of large myelin protein zero leads to Charcot-Marie-Tooth disease-like neuropathy in mice. Commun Biol 3:121.
Pelagalli A, Nardelli A, Lucarelli E, Zannetti A, Brunetti A (2018) Autocrine signals increase ovine mesenchymal stem cells migration through Aquaporin-1 and CXCR4 overexpression. J Cell Physiol 233:6241-6249.

Record CJ et al. (2023) Genetic analysis and natural history of Charcot-Marie-Tooth disease CMTX1 due to GJB1 variants. Brain 146:4336-4349.

Rydmark M, Berthold CH, Gatzinsky KP (1998) Paranodal Schwann cell mitochondria in spinal roots of the cat. An ultrastructural morphometric analysis. J Neurocytol 27:99-108.

Sanchez-de la Torre A, Aguado T, Huerga-Gomez A, Santamaria S, Gentile A, Chara JC, Matute C, Monory K, Mato S, Guzman M, Lutz B, Galve-Roperh I, Palazuelos J (2022) Cannabinoid CB(1) receptor gene inactivation in oligodendrocyte precursors disrupts oligodendrogenesis and myelination in mice. Cell death & disease 13:585.

Scherer SS, Xu YT, Nelles E, Fischbeck K, Willecke K, Bone LJ (1998) Connexin32-null mice develop demyelinating peripheral neuropathy. Glia 24:8-20.

Scherer SS, Xu YT, Messing A, Willecke K, Fischbeck KH, Jeng LJ (2005) Transgenic expression of human connexin32 in myelinating Schwann cells prevents demyelination in connexin32-null mice. J Neurosci 25:1550-1559.

Schneider CA, Rasband WS, Eliceiri KW (2012) NIH Image to ImageJ: 25 years of image analysis. Nat Methods 9:671-675.

Segura-Anaya E, Martinez-Gomez A, Dent MA (2015) Localization of aquaporin 1 water channel in the Schmidt-Lanterman incisures and the paranodal regions of the rat sciatic nerve. Neuroscience 285:119-127.

Stauch K, Kieken F, Sorgen P (2012) Characterization of the structure and intermolecular interactions between the connexin 32 carboxyl-terminal domain and the protein partners synapse-associated protein 97 and calmodulin. J Biol Chem 287:27771-27788.

Temperini C, Scozzafava A, Vullo D, Supuran CT (2006) Carbonic anhydrase activators. Activation of isoforms I, II, IV, VA, VII, and XIV with L- and D-phenylalanine and crystallographic analysis of their adducts with isozyme II: stereospecific recognition within the active site of an enzyme and its consequences for the drug design. J Med Chem 49:3019-3027.

Wang R, He J, Li JJ, Ni W, Wu ZY, Chen WJ, Wang Y (2015) Clinical and genetic spectra in a series of Chinese patients with Charcot-Marie-Tooth disease. Clin Chim Acta 451:263-270.

Wang YY, Chang RB, Liman ER (2010) TRPA1 is a component of the nociceptive response to CO2. J Neurosci 30:12958-12963.

Williams MM, Tyfield LA, Jardine P, Lunt PW, Stevens DL, Turnpenny PD (1999) HMSN and HNPP. Laboratory service provision in the south west of England--two years' experience. Ann N Y Acad Sci 883:500-503.

Zigo M, Kerns K, Sen S, Essien C, Oko R, Xu D, Sutovsky P (2022) Zinc is a master-regulator of sperm function associated with binding, motility, and metabolic modulation during porcine sperm capacitation. Commun Biol 5:538.

Figures and legends

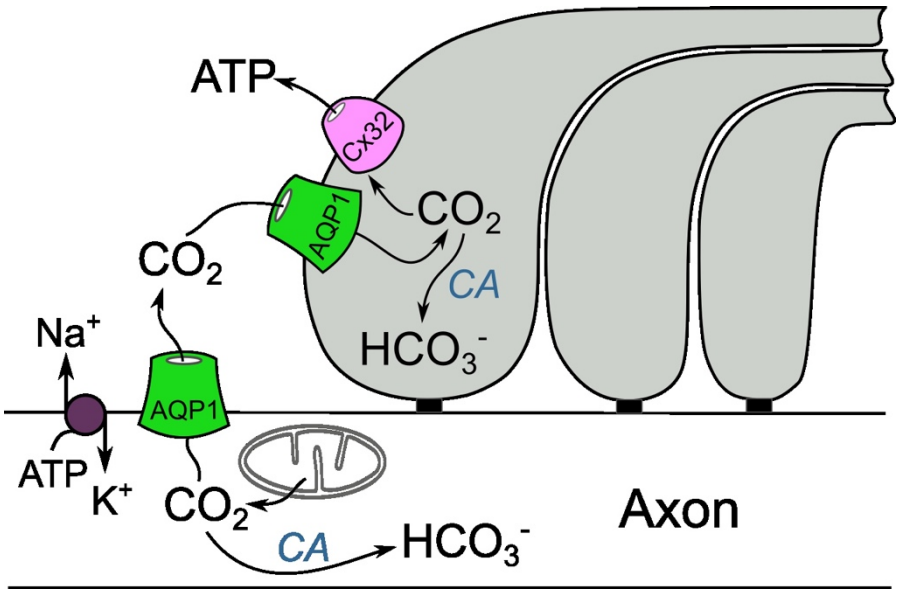

Figure1. Hypothesised Cx32 mediated CO_2 signalling cascade in peripheral myelin. Three fingers of a myelin paranode have been used for illustrative purposes. Restoration of transmembrane ionic gradients following action potential propagation via the actions of Na^+/K^+ ATPases incurs a metabolic cost and increases production of ATP and CO_2. AQP1, permeable to CO_2, provides a pathway for CO_2 to leave the node and enter the paranode and bind to Cx32 on the intracellular loop. This triggers opening of Cx32 and release ATP. Carbonic anhydrase (CA) catalyzes the combination of CO_2 and H_2O and ultimately the production of HCO_3^- and H^+ ions and effectively competes with Cx32 for CO_2.

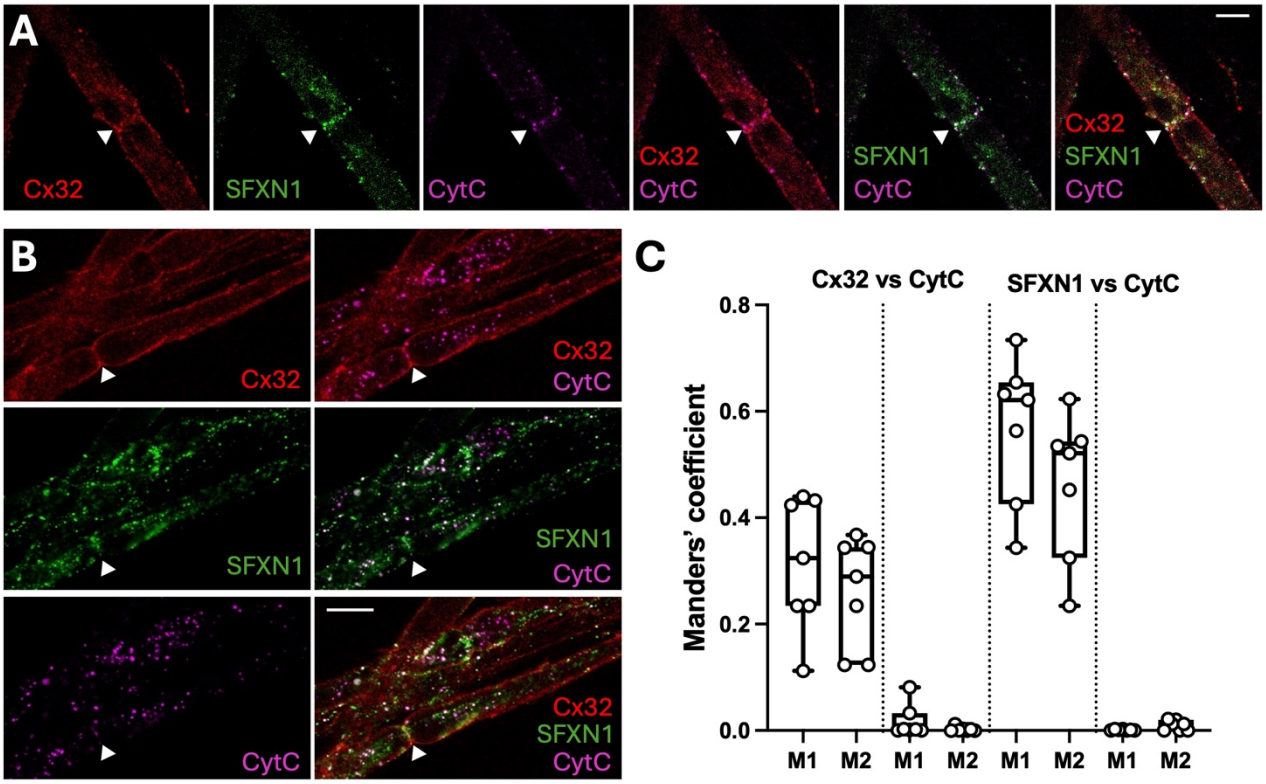

Figure 2. Cx32 colocalises with mitochondria in the Schwann cell paranode, alongside SFXN1. A, B) Representative images showing the localisation of Cx32, CytC and SFXN1 in isolated mouse sciatic nerve. Arrowheads depict the node. Scale bars – 10µm. C) Boxplots showing degree of colocalization between Cx32 and CytC and SFXN1 and CytC. M1 is the proportion of Cx32 (or SFXN1) that colocalises with CytC and M2 is the reverse proportion of CytC that colocalises with Cx32 (or SFXN1). Control measurements used these same images with one channel flipped 90° right and the same thresholds as when measuring colocalization. Kruskal Wallis ANOVA: Cx32 vs CytC, $p = 0.0001$; SFXN1 vs CytC, $p < 0.0001$.

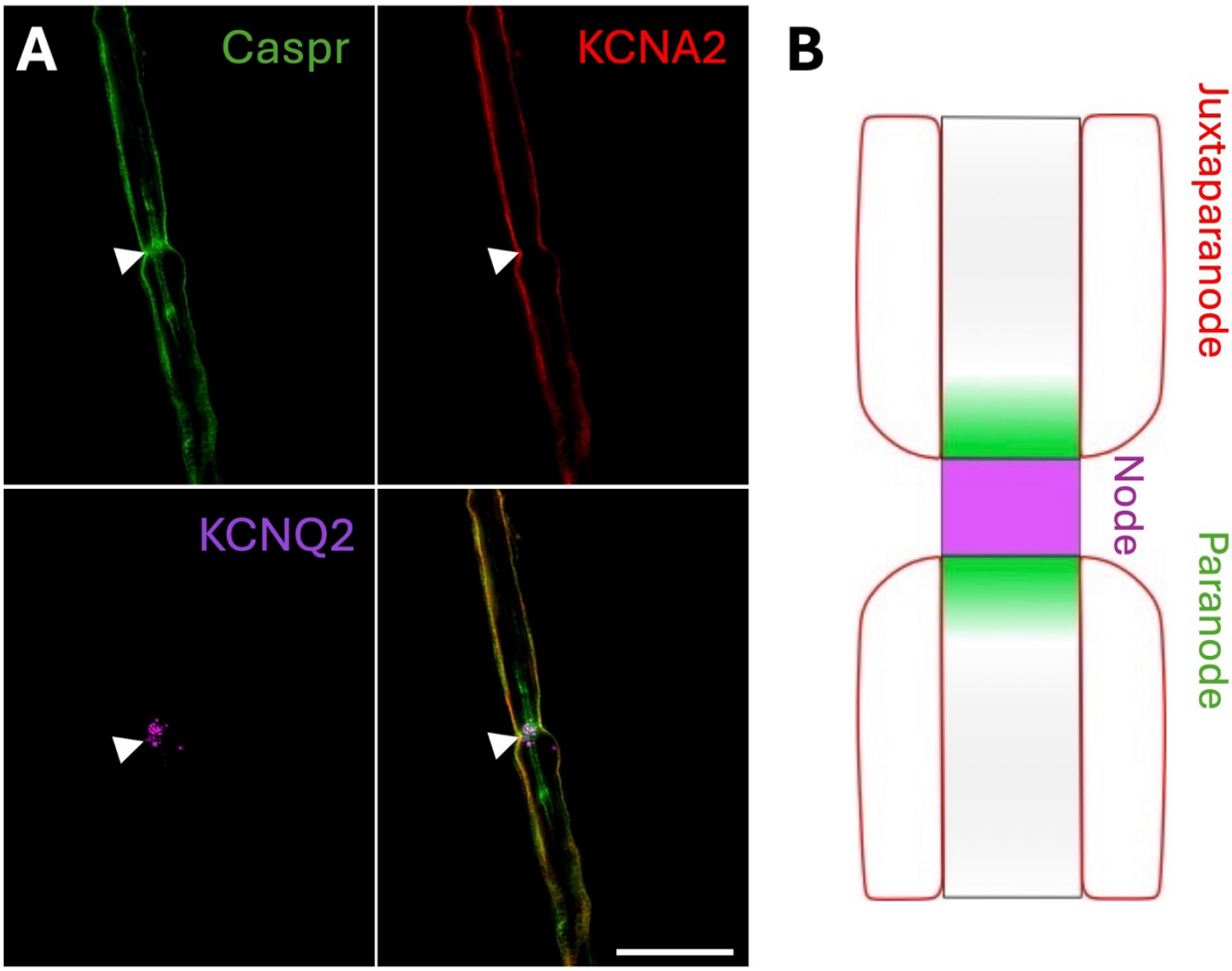

Figure 2 figure supplement 1. Markers for the node, paranode and juxtaparanode in the isolated mouse sciatic nerve. A) Location of the axonal node (KCNQ2) and Schwann cell paranode (Caspr) within an isolated mouse sciatic nerve fibre. KCNA2 is expressed in the outer myelin layer. Arrowheads indicate the node. Scale bar = 15 μm. B) Schematic indicating the same locations within an isolated nerve fibre.

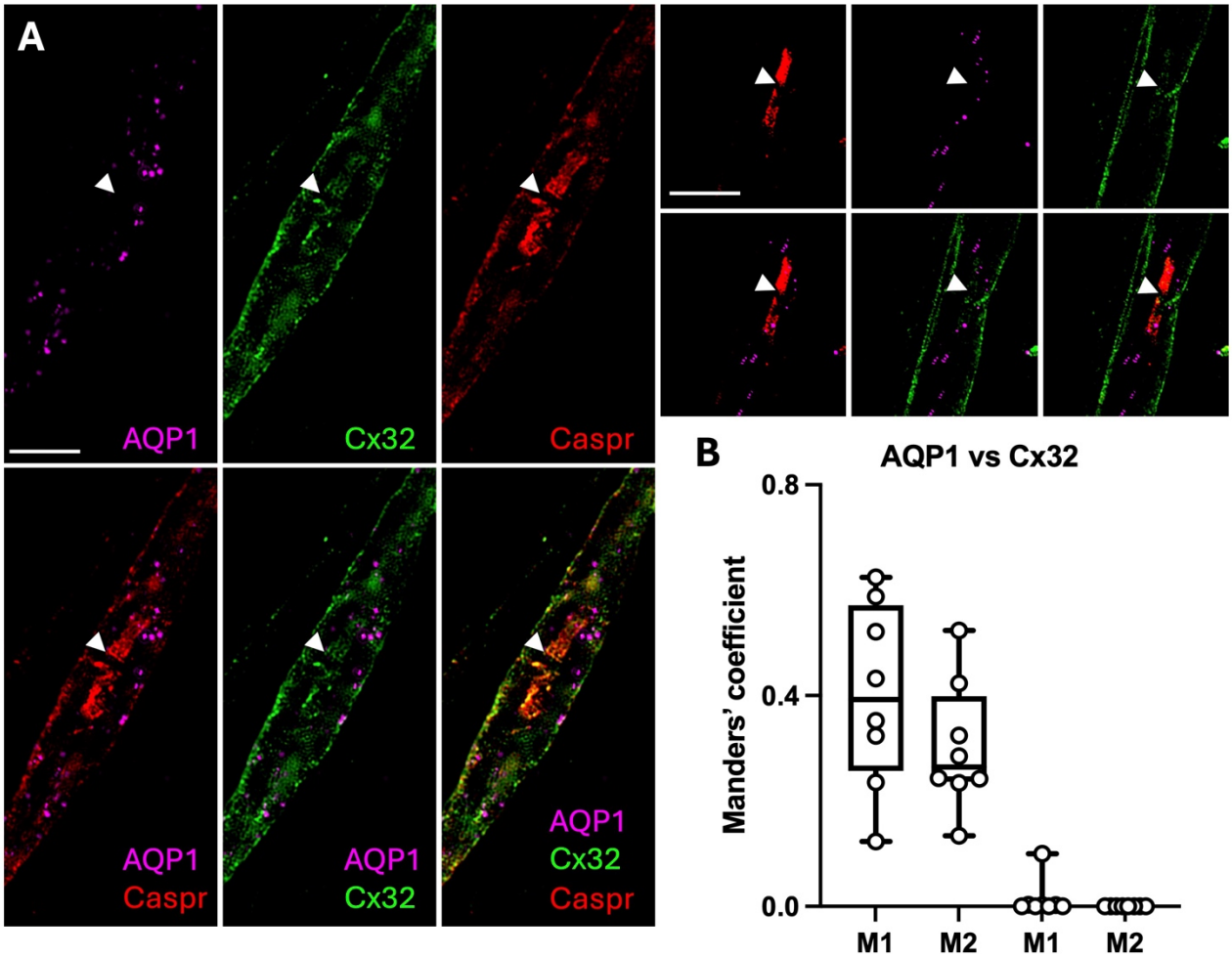

Figure 3. AQP1 localizes to both the Schwann cell paranode and also the axonal node. A) Representative images showing the localisation of Caspr, Cx32 and AQP1 in isolated mouse sciatic nerve. Arrowheads indicate the node. Scale bars, 10 µm. B) Boxplots showing degree of colocalization between Cx32 and AQP1. Kruskal Wallis ANOVA $p < 0.0001$.

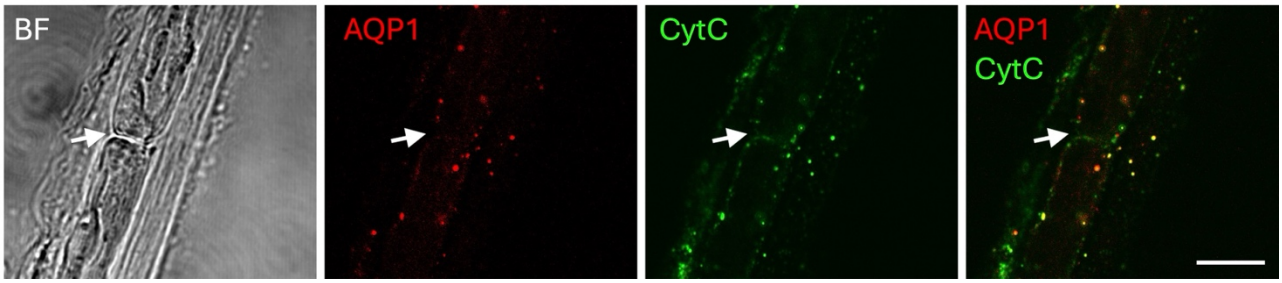

Figure 3 figure supplement 1. The localization of AQP1 in relation to mitochondria, CytC, in isolated mouse sciatic nerve. Representative images showing the localisation of AQP1 and CytC in isolated mouse sciatic nerve. Arrows indicate the node. Scale bar – 10μm.

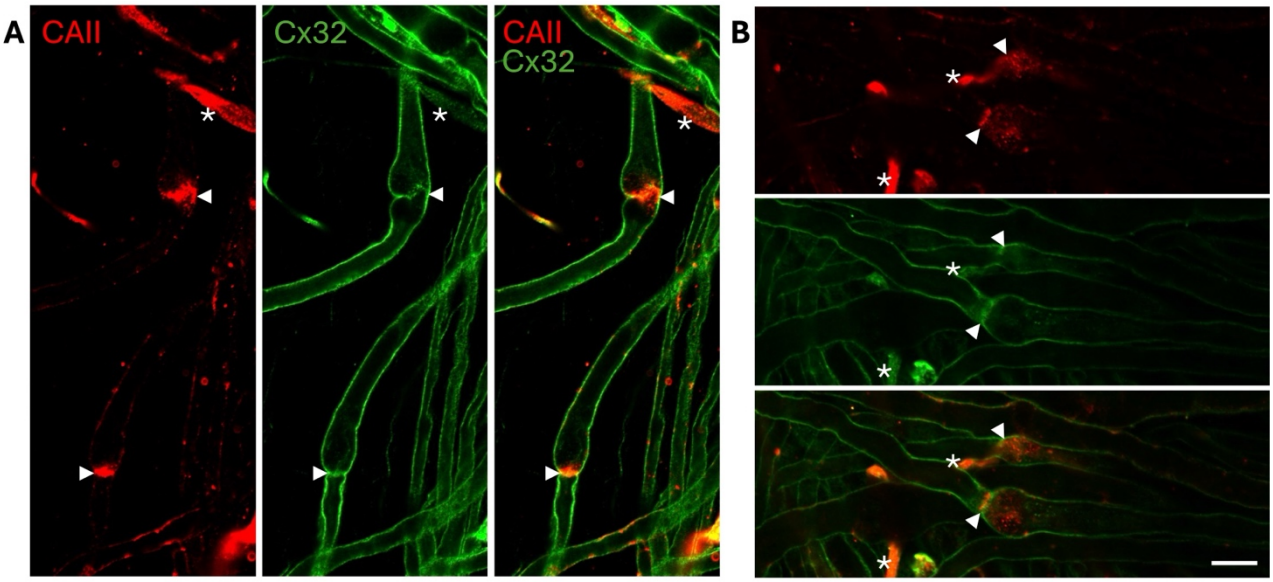

Figure 4: CAII localizes to myelinating Schwann cells, in particular to the axonal node and the Schwann cell paranode. (A and B) Representative images showing the localisation of CAII and Cx32 in isolated mouse sciatic nerve. Arrow heads indicate the node, and arrows depict the outer myelin. Intense CAII staining, denoted by a white asterisk (*) is present in non-myelinated fibres. Scale bar applies to A and B: 10μm.

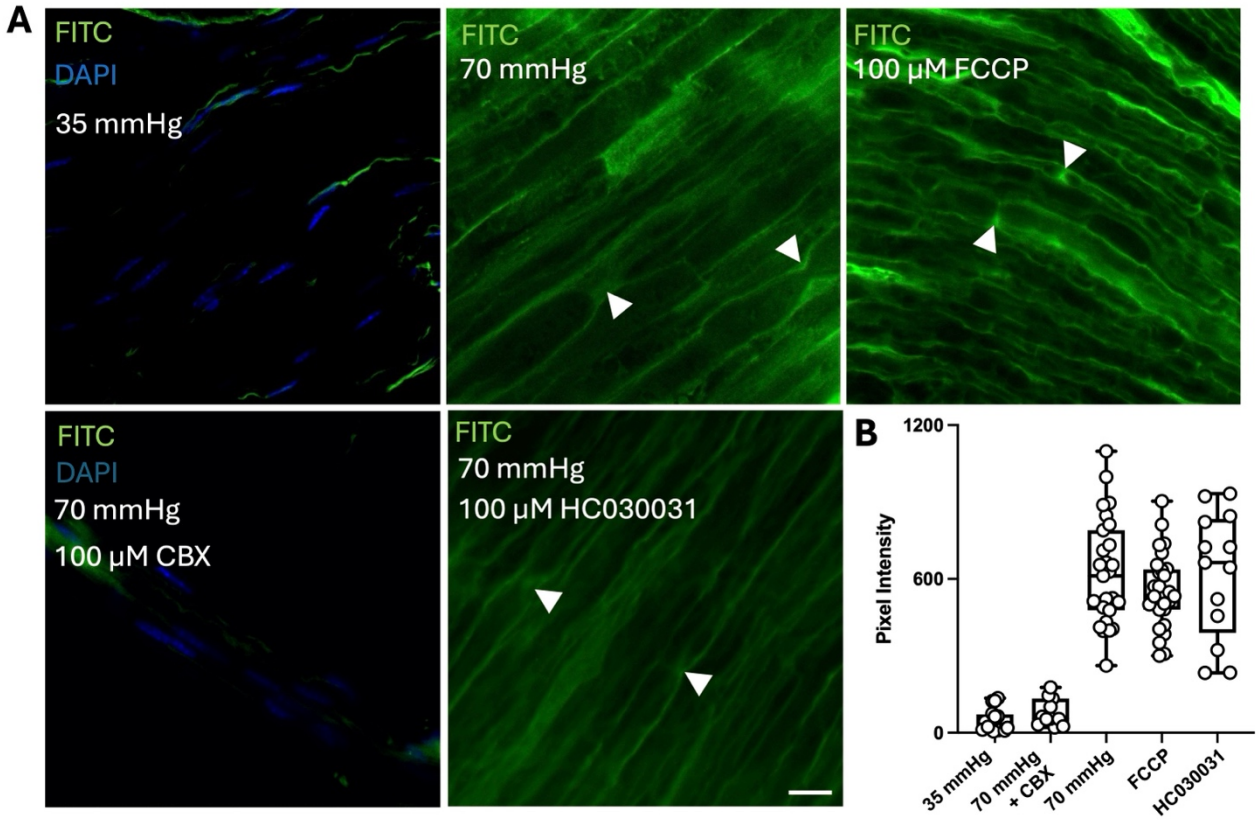

Figure 5: A membrane impermeable dye, FITC, loads into Schwann cell paranodes in a CO_2 dependent manner through a hemichannel. A) Representative images showing the FITC loading into mouse sciatic nerve bundles. Arrow heads indicate the node. Little FITC loading occurs in response to control (35mmHg) aCSF. FITC loading was greatly increased by 70 mmHg aCSF and application of 100 μM FCCP. FITC loading in 70 mmHg aCSF was blocked by carbenoxolone (CBX) but not the TRPA1 antagonist HC030031. B) Boxplot showing intensity of FITC fluorescence under the different conditions. Each point represents a separate ROI from 5 different nerves for each condition. Scale bar – 10μm.

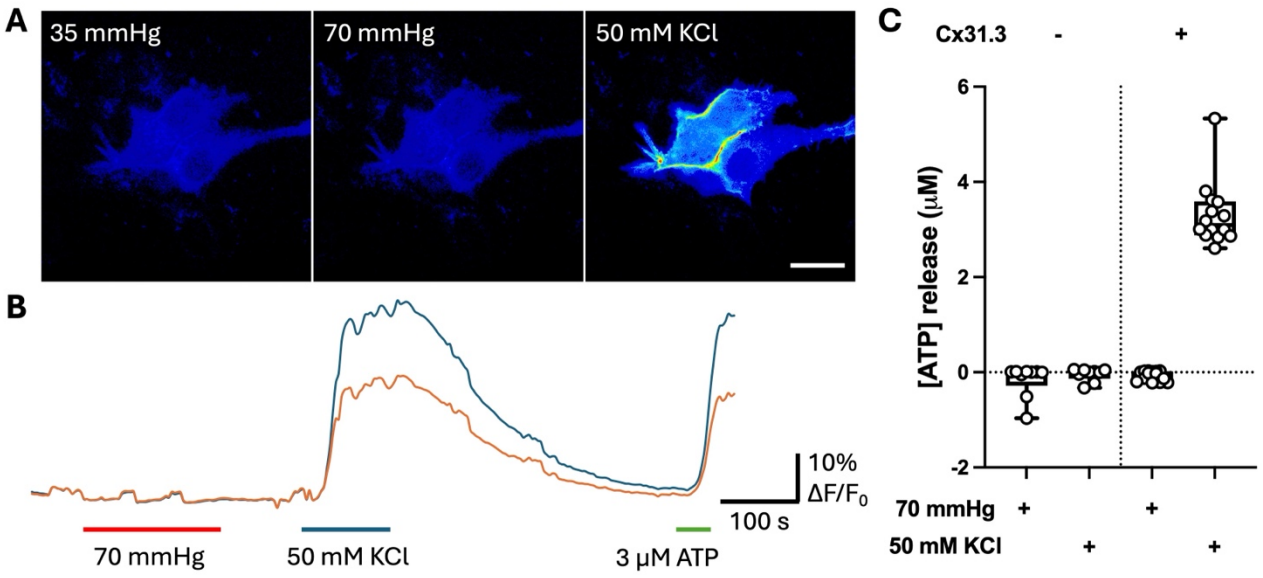

Figure 5 figure supplement 1: Cx31.3 does not open in response to hypercapnia. A) Representative images of $GRAB_{ATP}$ fluorescence, encoded by a 16 colour LUT in Cx31.3 transfected HeLa cells in response to control (35 mmHg), hypercapnic (70 mmHg) and depolarising (50 mM KCl) aCSF. Scale bar 20 µm. B) Trace showing the change in normalised $GRAB_{ATP}$ fluorescence from the cells shown in (A). C) Summary statistic box plots showing the [ATP] release, calculated as a ratio from the normalised fluorescence change evoked by a certain solution or stimuli and the fluorescence change evoked by 3 µM ATP. Cells expressing only $GRAB_{ATP}$ do not exhibit changes in fluorescence to 70 mmHg or 50 mM KCl aCSF. Each data point represents a cell, with all cells coming from at least three transfections.

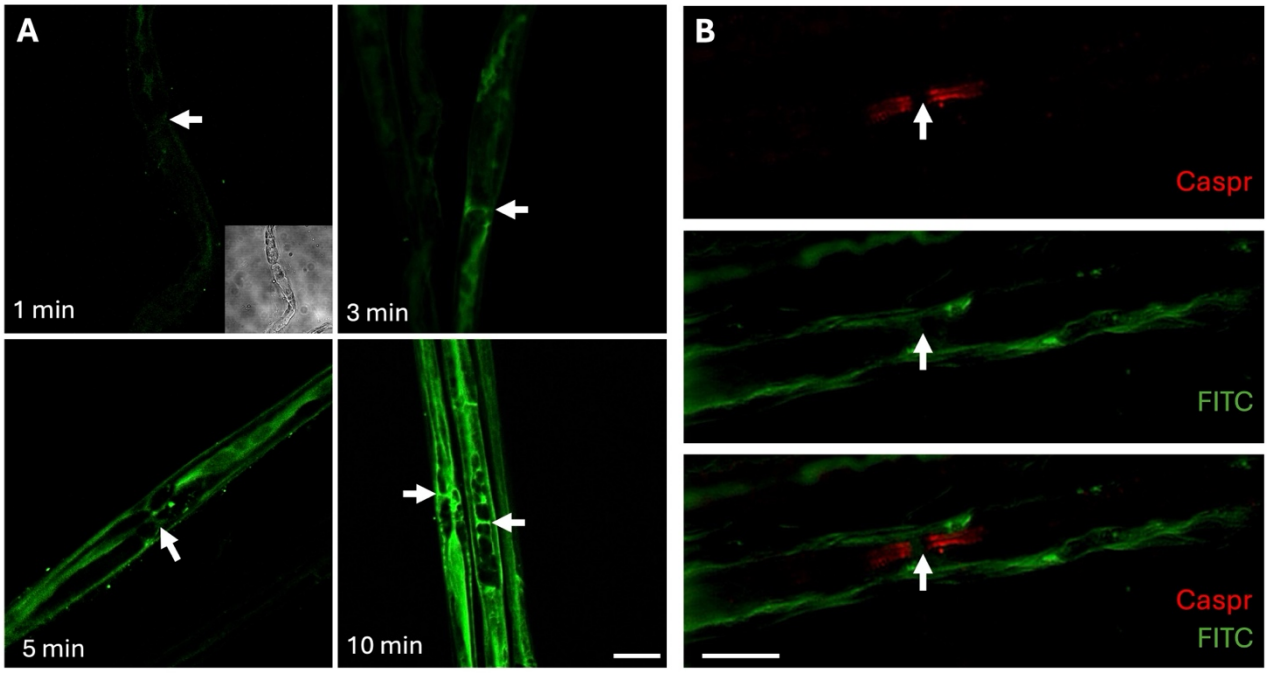

Figure 6: Activity dependent loading of FITC into Schwann cell paranodes. A) Representative images showing the FITC loading into mouse sciatic nerve bundles in response to different lengths of stimulation (30 Hz). Arrows indicate the paranode. B) An isolated mouse sciatic nerve fibre loaded with the membrane impermeable dye FITC and counterstained with Caspr, an axonal membrane protein which is expressed only in the paranodal region. White arrows indicate the paranode of interest. Note lack of loading into the axon. Scale bars – 15 µm.

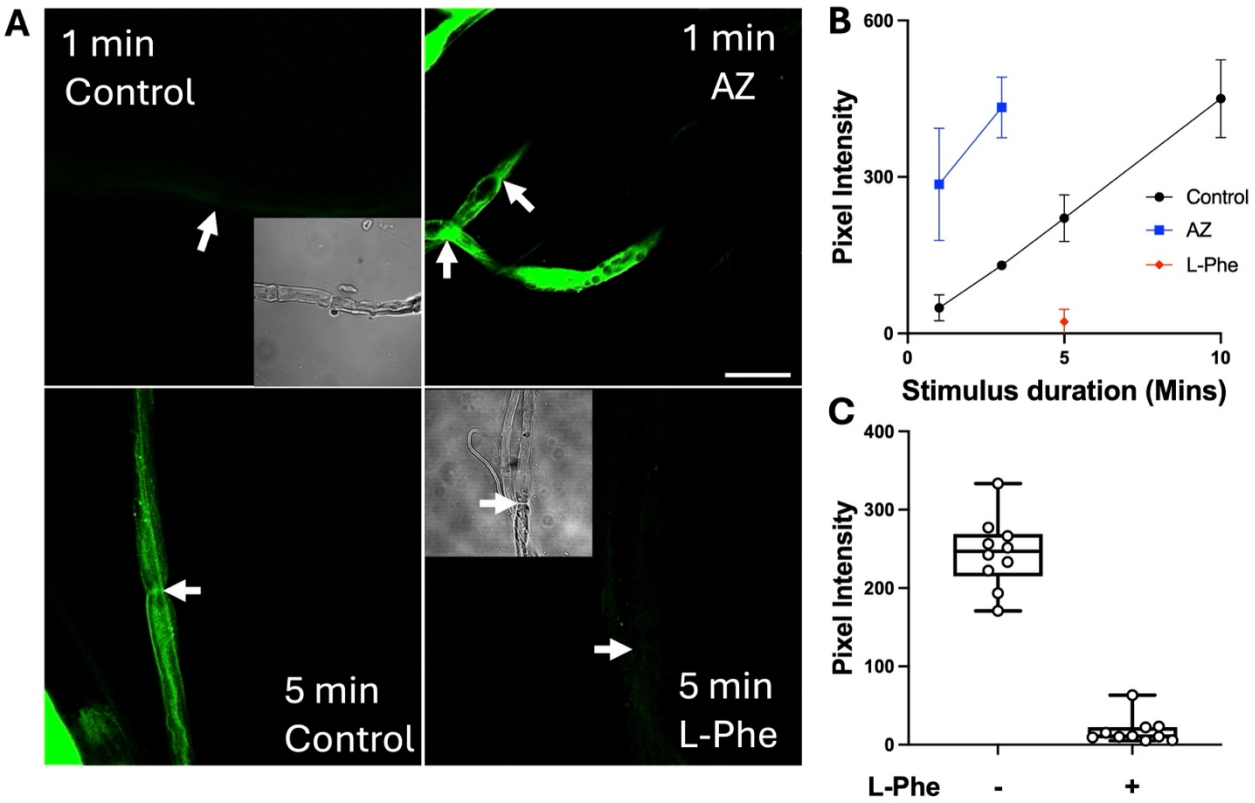

Figure 7: Activity dependent loading of FITC is sensitive to manipulation of carbonic anhydrase activity. A) Representative images showing the FITC loading into mouse sciatic nerve bundles in response to 1 min of electrical stimulation in the absence (left) or presence (right) of the carbonic anhydrase inhibitor, acetazolamide. Arrowheads indicate the position of paranodes. Brightfield inset shows the presence of the nerve fibre and the arrowhead in the fluorescence image indicates its position. B) Summary plot showing how the pixel intensity of Schwann cell paranodes, and therefore FITC loading, vary in response to stimulus duration and the presence of acetazolamide (each point mean ± SD). C) Representative images showing the FITC loading into mouse sciatic nerve bundles in response to five minutes of stimulation in the absence (left) or presence (right) of the carbonic anhydrase enhancer, L-Phenylalanine. Brightfield inset shows the presence of the nerve fibre and the arrowhead in the fluorescence image indicates its position. D) Boxplot showing the effect L-Phenylalanine had on FITC loading into mouse Schwann cell paranodes. Scale bars – 15 µm. Each point represents a separate ROI from 5 different nerves. L-Phe vs control MW U test: $p<0.0001$.

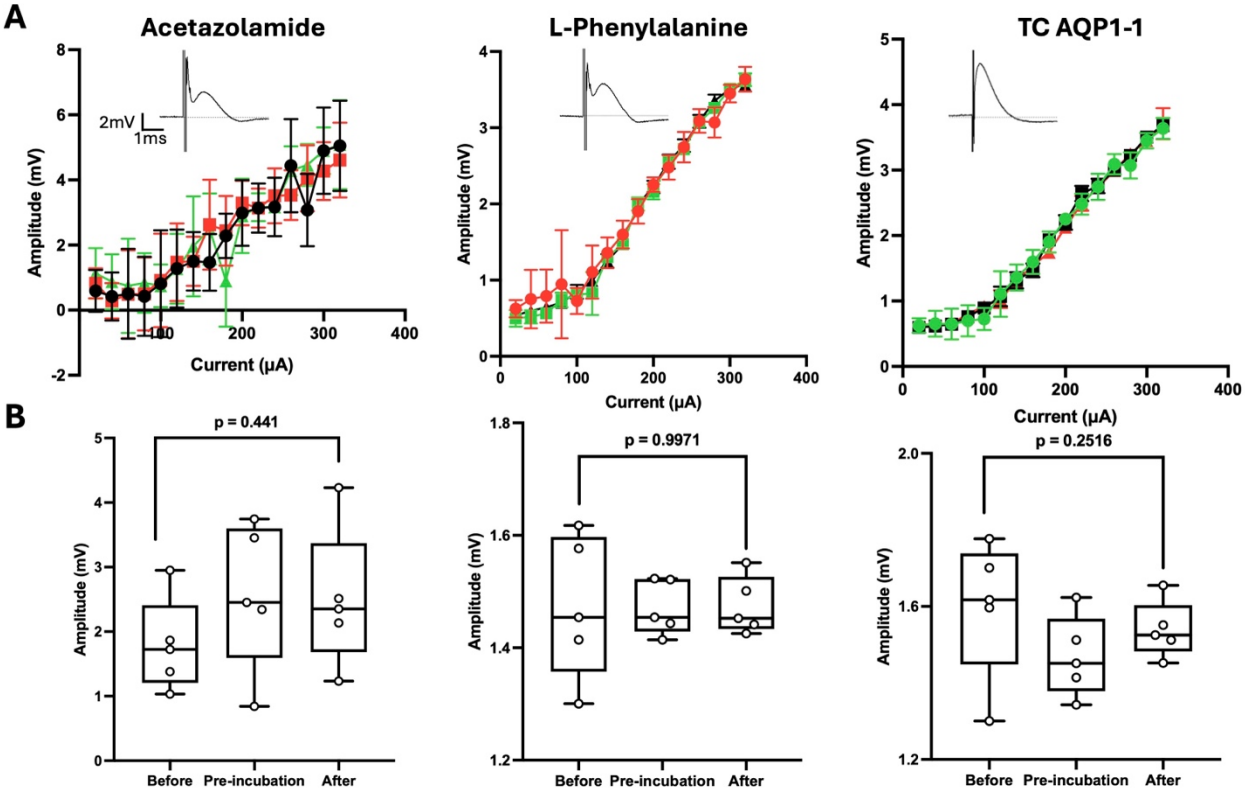

Figure 7 figure supplement 1. Acetazolamide, TC AQP1-1 and L-Phe do not alter the CAP. A) Cumulative current –voltage curves, comprising data from all nerves subjected to either 100 µM acetazolamide (left),1 mM L-Phenylalanine (middle) or 80 µM TC AQP1-1 (right). Curves were produced before application of the respective compound, at the end of the pre-incubation of the compound and at the end of dye loading to show the compound itself had no effect on the morphology of the CAP. N=5 nerves for each condition. B) Boxplots showing the half maximum CAP amplitude for each respective condition and compounds laid out in (A). Kruskal Wallis ANOVA: Acetazolamide, p = 0.4441; L-Phenylalanine, p = 0.9917; TC AQP1-1, p = 0.2516

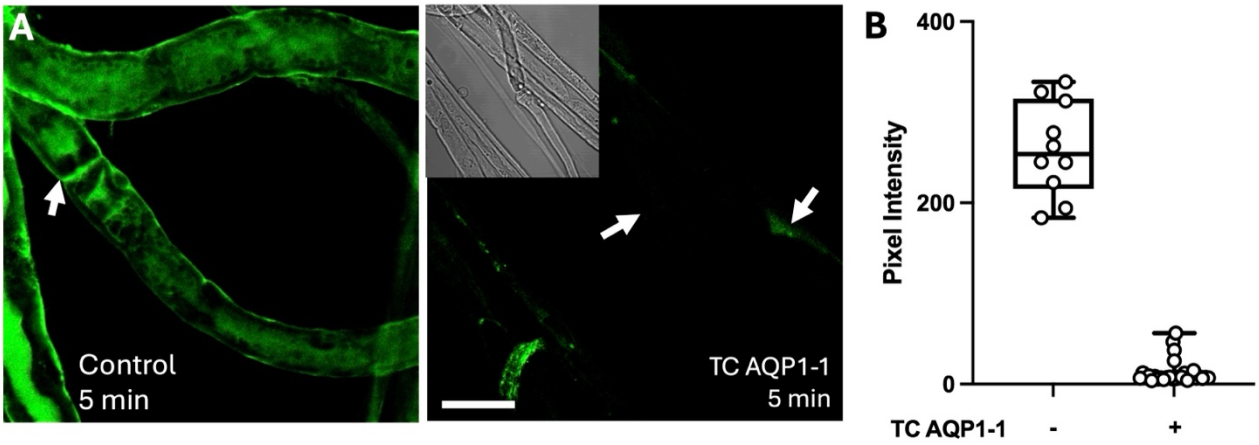

Figure 8. Activity dependent loading of the FITC is reduced by inhibition of AQP1. A) Representative images showing the FITC loading into mouse sciatic nerve bundles in response to 5 minutes of 30 Hz stimulation in the absence (left) or presence (right) of the AQP1 blocker TC AQP1-1. Brightfield inset shows the presence of the nerve fibre and the arrows in the fluorescence images indicates position of paranodes. Scale bar – 15 µm. B) Boxplot showing the effect TC AQP1-1 had on FITC loading into mouse Schwann cell paranodes. Each point represents a separate ROI from 5 different nerves. TC AQP1-1 vs control MW U test: $p<0.0001$.

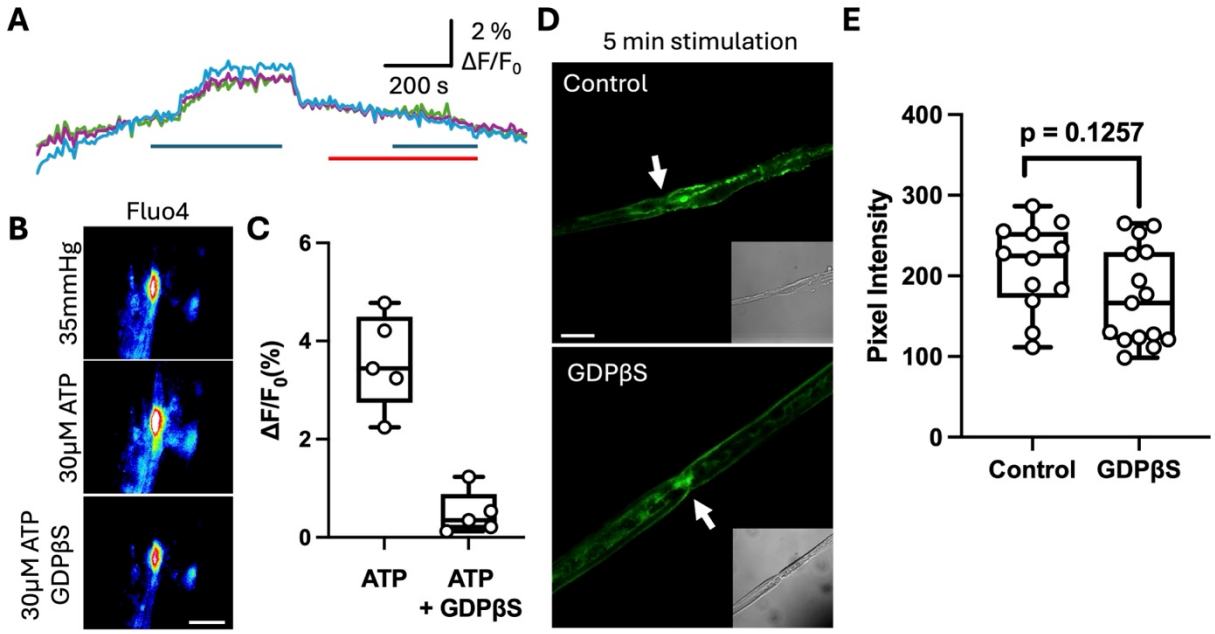

Figure 8 figure supplement 1. GDPβS blocks ATP-induced increases in paranodal Ca^{2+} but does not alter activity dependent FITC loading into the paranode. A) Recording of ATP-induced increase in intracellular Ca^{2+} at the paranode (blue bar). When ATP was applied after 100 μM GDPβS (red bar), no increase in Fluo4 fluorescence was seen. B) Images of Fluo4 fluorescence showing effect of ATP with and with GDPβS (same recording as A). Scale bar = 5 μm. C) Boxplots summarizing that GDPβS blocks the change in fluorescence induced by ATP. Each point is a single paranode from a single nerve. D) Images of FITC loading into sciatic nerve induced by 5 min electrical stimulation with and without 100 μM GDPβS. Arrows point to paranode, insets show corresponding brightfield images. Scale bar 10 μm. E) Boxplots showing that GDPβS has no effect on activity dependent (30 Hz stimulation) FITC loading. Each point represents a separate ROI from 5 different nerves.

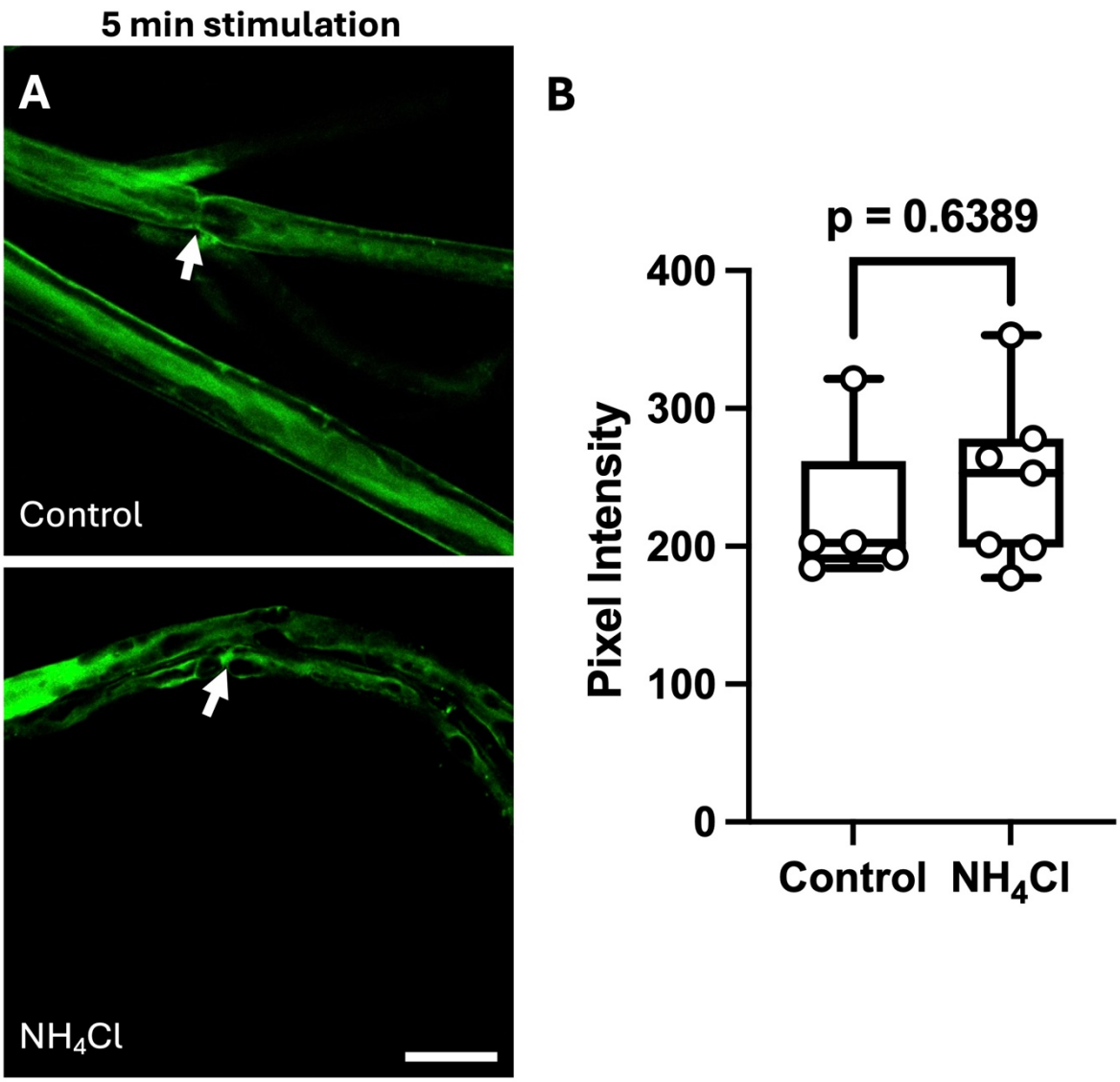

Figure 8 figure supplement 2. NH_4Cl does not alter FITC loading into the paranode. A) Images of FITC fluorescence in isolated nerves stimulated for 5 minutes at 30 Hz, in the control (35 mmHg) and after treatment with 100 μM NH_4Cl. Arrows indicate paranode. Scale bar 15 μm. B) Summary graph of FITC fluorescence in nerves in response to 5 minutes stimulation in each condition. Each point represents a separate ROI from 5 different nerves.

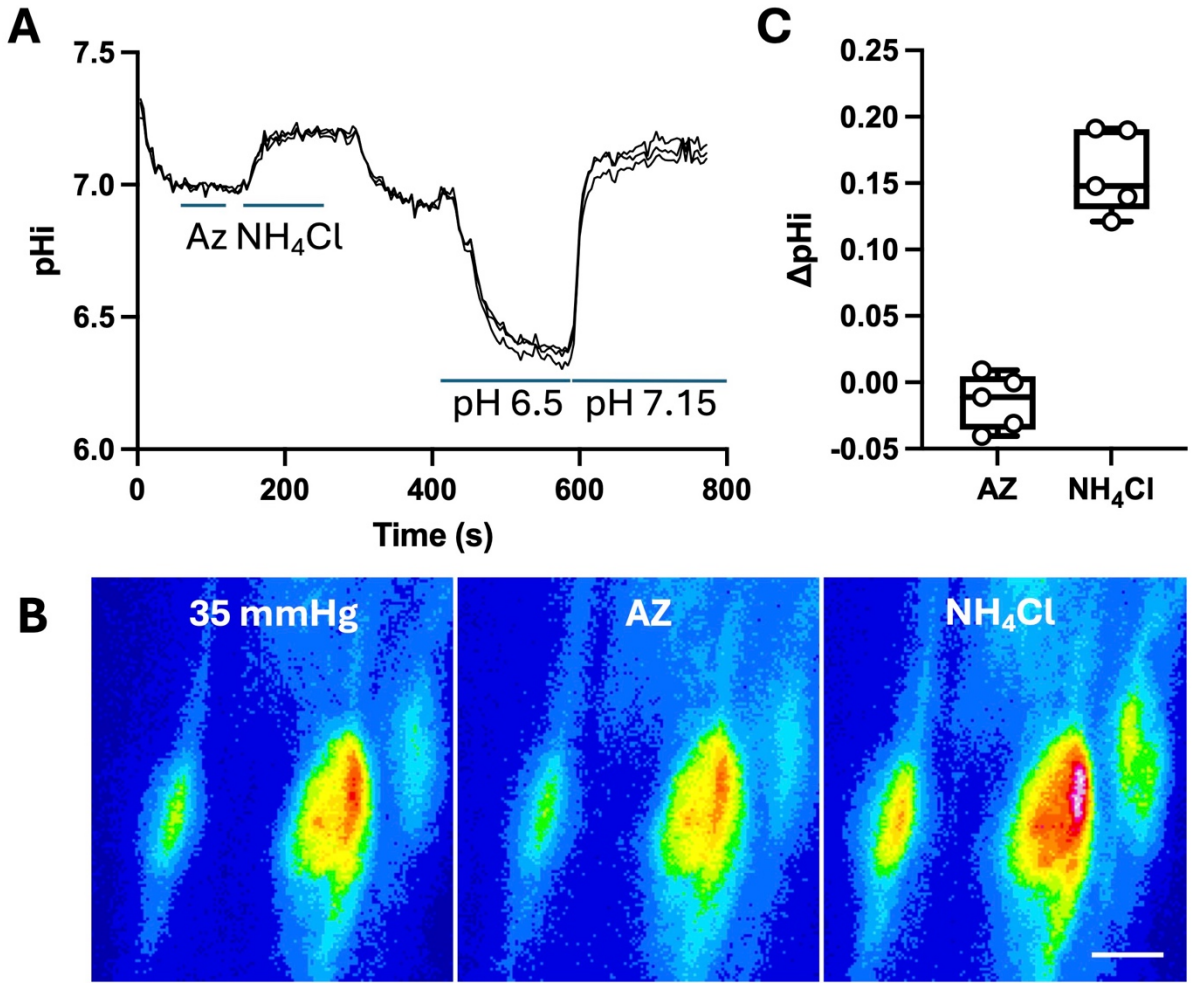

Figure 8 figure supplement 3. Effects of acetazolamide and NH_4Cl on the intracellular pH of Schwann cell paranodes. A) representative trace showing the normalised BCECF fluorescence $\Delta F/F_0$ in response to changing pH to 6.5 and 7.15, 100μM acetazolamide (AZ) and 100 μM NH_4Cl. B) representative images for the trace for the BCECF fluorescence in each condition. Scale bar = 5 μm. C) Summary graph of effect of AZ and NH_4Cl on intracellular pH. Each point represents a nerve.

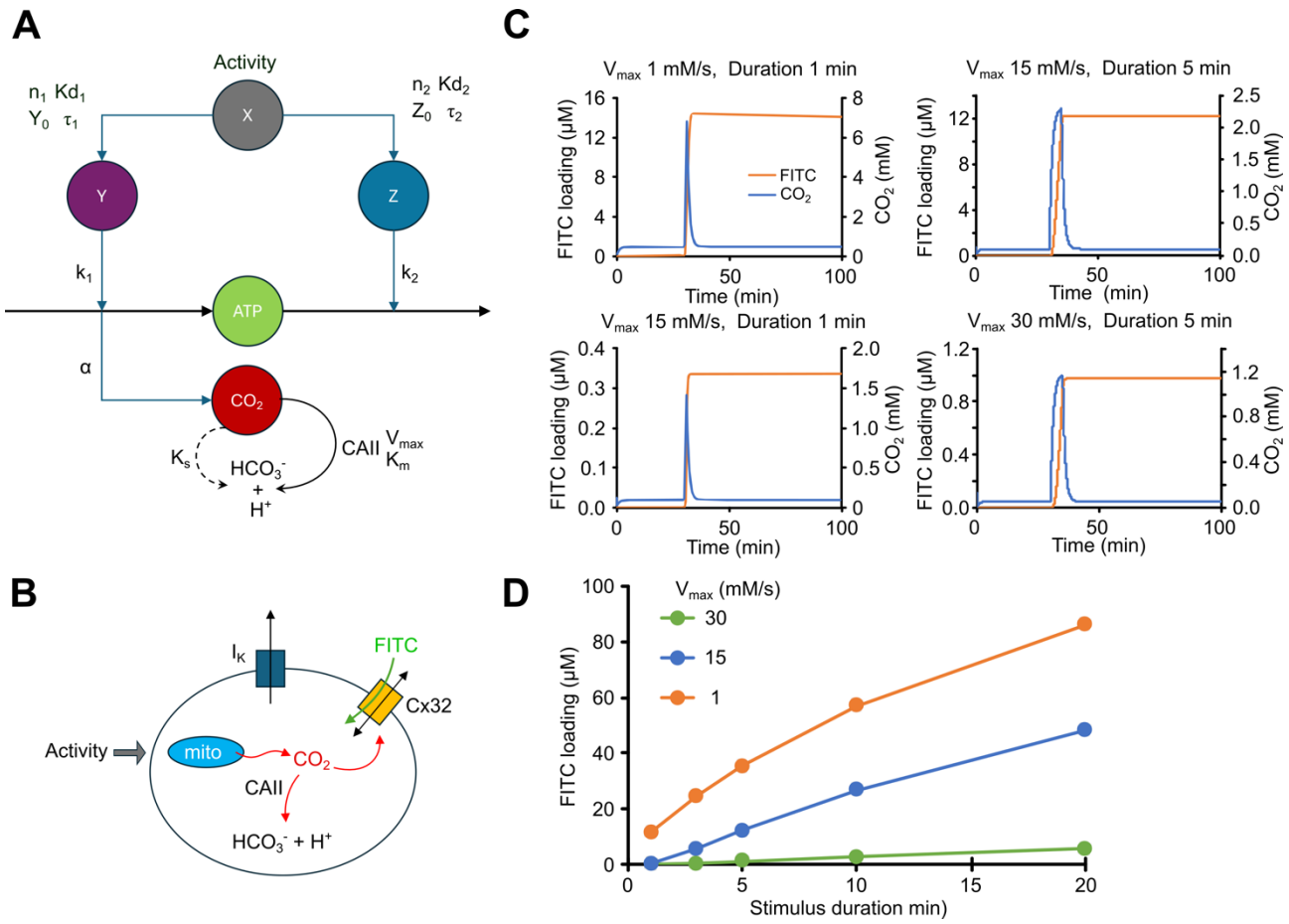

Figure 9: Simple model of CO_2 signalling at the paranode reproduces experimentally observed patterns of activity dependent FITC loading. A) Adaptation of the Matsuda et al model to incorporate CO_2 production and metabolism via CAII. Action potentials provide the input to the model as activity variable X, which determines variables Y and Z, which determine ATP production and consumption. CO_2 is proportional to ATP production, via the rate constant α. Code for the model is provided in the Matlab files CO2Cx32Model.m and CO2Cx32Plot.m. B) Incorporation of the modified Matsuda et al model into a single cell that possesses a K^+ leak channel and Cx32 and represents the paranode, albeit including the nodal mitochondria. (C) Outputs from the model to show how the change in [CO_2] and the consequent FITC loading evoked by two different durations of stimulation (1 and 5 min) varies with the V_{max} of CAII. Reduction from the control value (15 mM/s) to 1 mM/s simulates the effect of acetazolamide, whereas an increase of V_{max} to 30 mM/s simulates application of L-Phe. D) A summary graph showing how FITC loading varies with stimulus duration with the 3 different values for the V_{Max} of CAII.

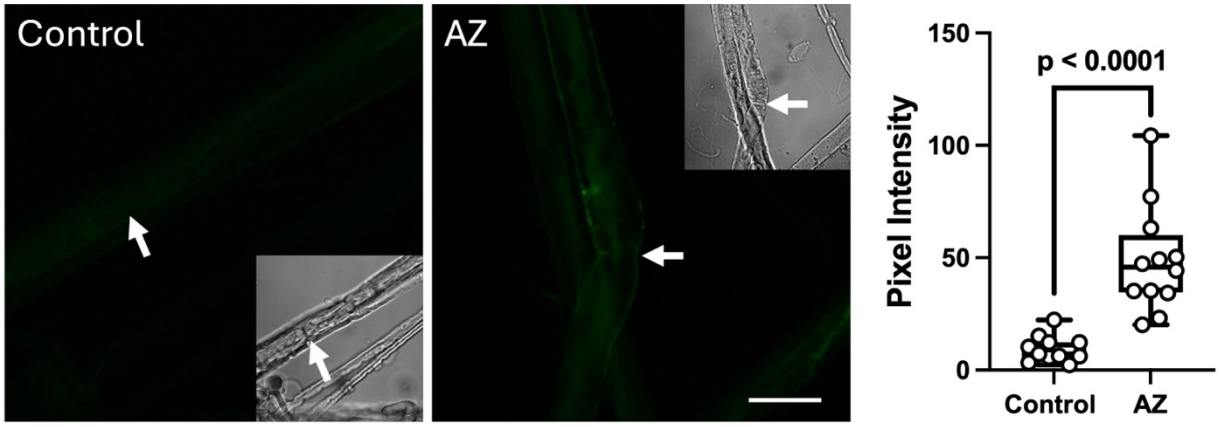

Figure 9, figure supplement 1. Inhibition of carbonic anyhydrase increases loading of FITC into paranodes and outer myelin in the absence of electrical stimulation. The images show the FITC fluorescence in the control and presence of 100 μM acetazolamide (AZ). The boxplot shows quantification of the fluorescence and that the increase in background fluorescence is significant (Mann Whitney U test). Each point represents a separate ROI from 5 different nerves.

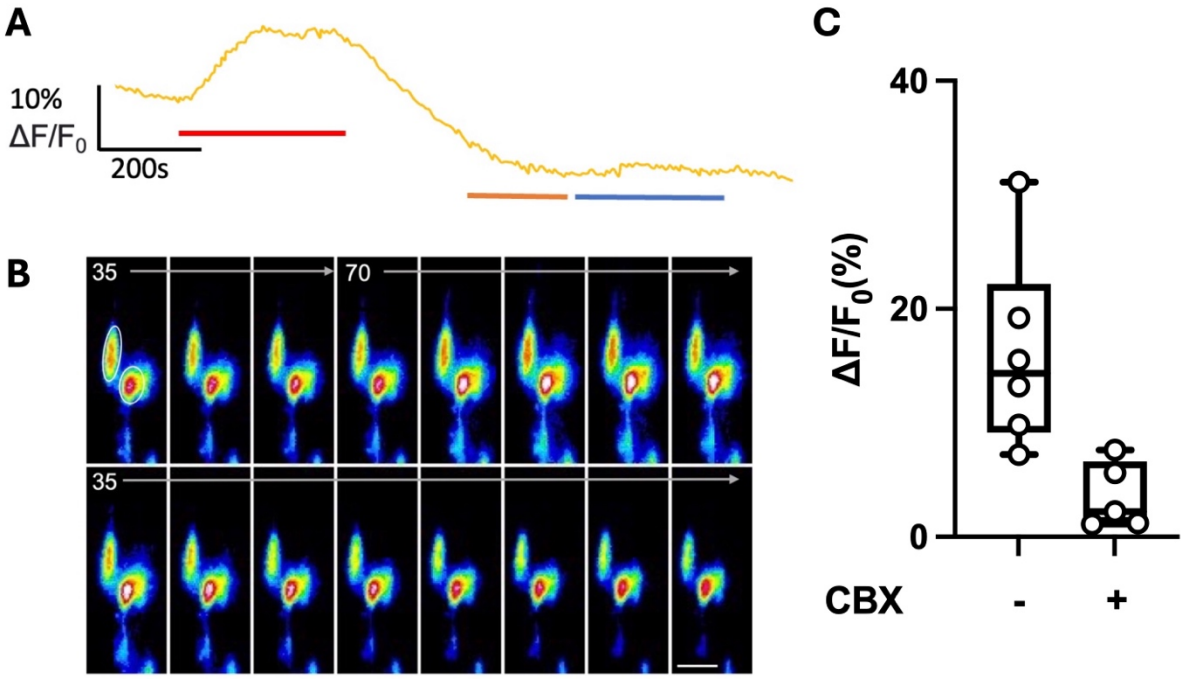

Figure 10: CO_2 dependent Ca^{2+} influxes into Schwann cell paranodes are hemichannel dependent. A) Representative trace showing change in normalised Fluo4 fluorescence in response to 70mmHg aCSF (red bar), 35mmHg aCSF with the non-specific hemichannel blocker carbenoxolone (100 µM, orange bar) and 70 mmHg aCSF plus 100 µM carbenoxolone (blue bar). B) Representative images showing changes Fluo4 fluorescence in response to hypercapnic aCSF. The circles in the first panel show the measurement ROIs drawn around the paranodes. Scale bar = 10 µm. C) Boxplot showing the change in normalised fluorescence ($\Delta F/F_0$) evoked in Fluo4 loaded Schwann cell paranodes in the presence and absence of100 µM carbenoxolone (CBX). Each datapoint consists of a paranode, with all the data collected from 4 sciatic nerves. Mann Whitney U test, $p = 0.0087$.

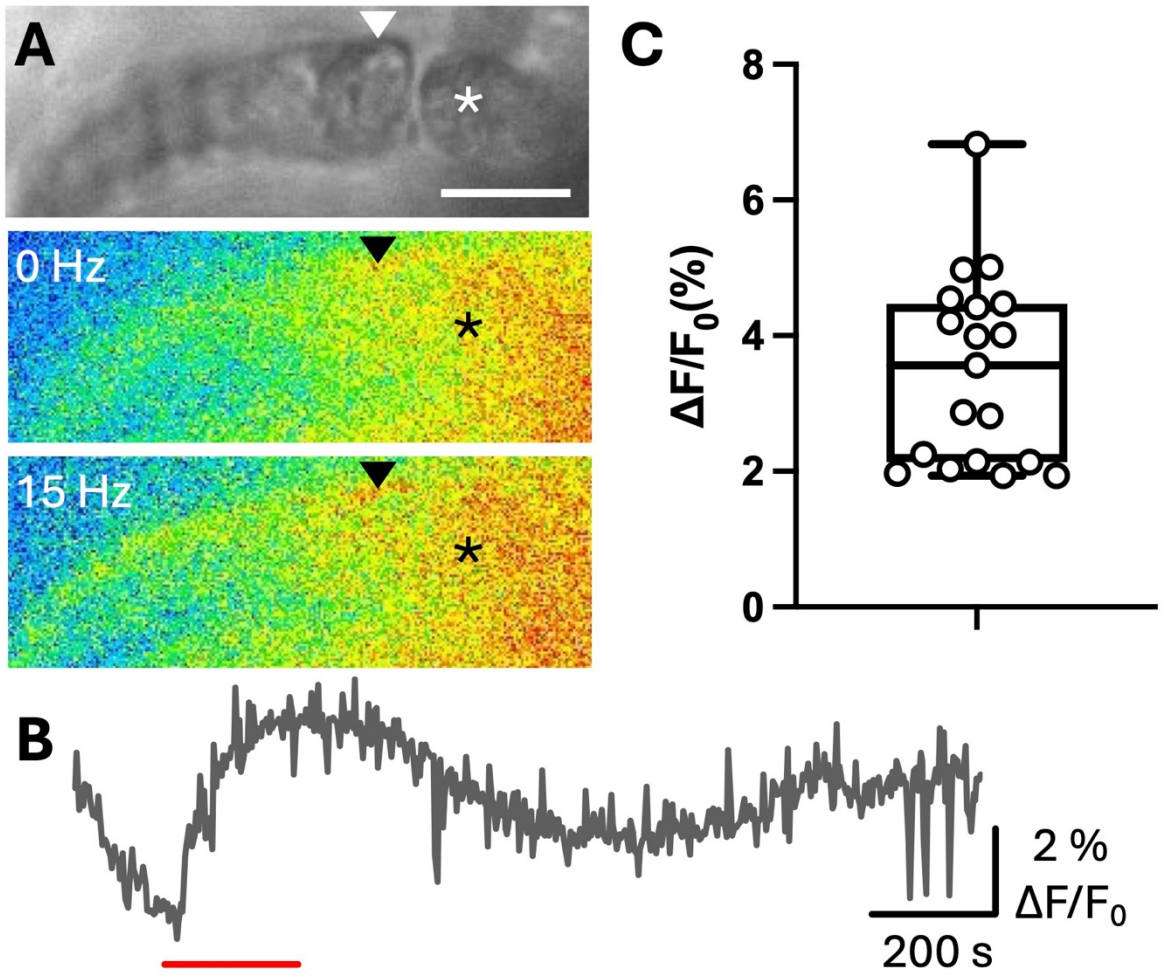

Figure 11: Activity dependent increase of intracellular Ca^{2+} in Schwann cell paranodes. A) Brightfield and fluorescence images of Fluo4 loaded nerve. The fluorescence images show before (0 Hz) and during stimulation of the nerve (15 Hz). An increase in fluorescence is evident in each paranode (arrowhead and asterisk). Scale bar = 5 µm. B) Representative trace showing change in normalised Fluo4 fluorescence in response to 15 Hz electrical stimulation (red bar). (C) boxplot showing the change in normalised fluorescence ($\Delta F/F_0$) evoked in Fluo4 loaded Schwann cell paranodes in response to 15 Hz electrical stimulation. Each datapoint consists of a paranode, with all the data collected from 4 sciatic nerves.

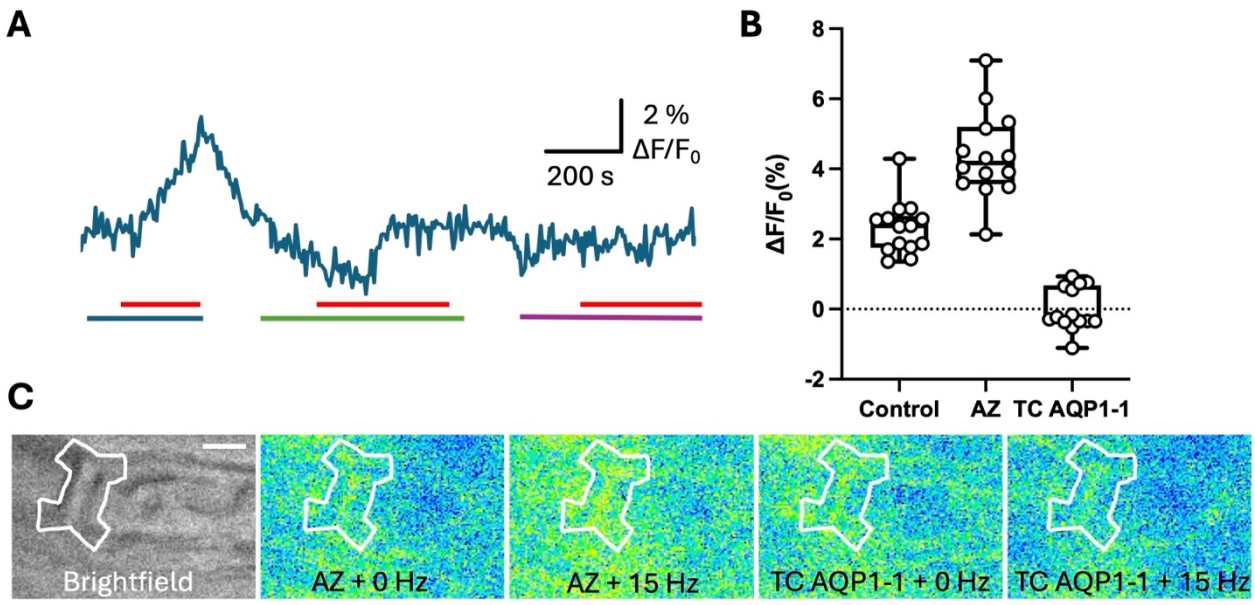

Figure 12. Activity dependent Ca^{2+} influxes into Schwann cell paranodes are dependent on CO_2. A) Representative trace showing change in normalised Fluo4 fluorescence in response to 15 Hz electrical stimulation (red bar) in the presence of 100 µM acetazolamide (blue bar), in control aCSF (green bar), or in the presence of 80 µM TC AQP1-1 (purple bar). B) Boxplot showing the change in normalised fluorescence ($\Delta F/F_0$) evoked in Fluo4 loaded Schwann cell paranodes in response to high frequency electrical stimulation in each condition. Each datapoint consists of a paranode, with all the data collected from 4 sciatic nerves. Kruskal Wallis ANOVA, $p < 0.0001$. Pairwise MW comparisons: control vs AZ, $p < 0.001$; control vs TC AQP1-1, $p<0.001$. C) Brightfield and fluorescence images showing the activity dependent Ca^{2+} increase in a paranode in the presence of acetazolamide (AZ) and the lack of an activity dependent increase in Ca^{2+} in the presence of TC AQP1-1.

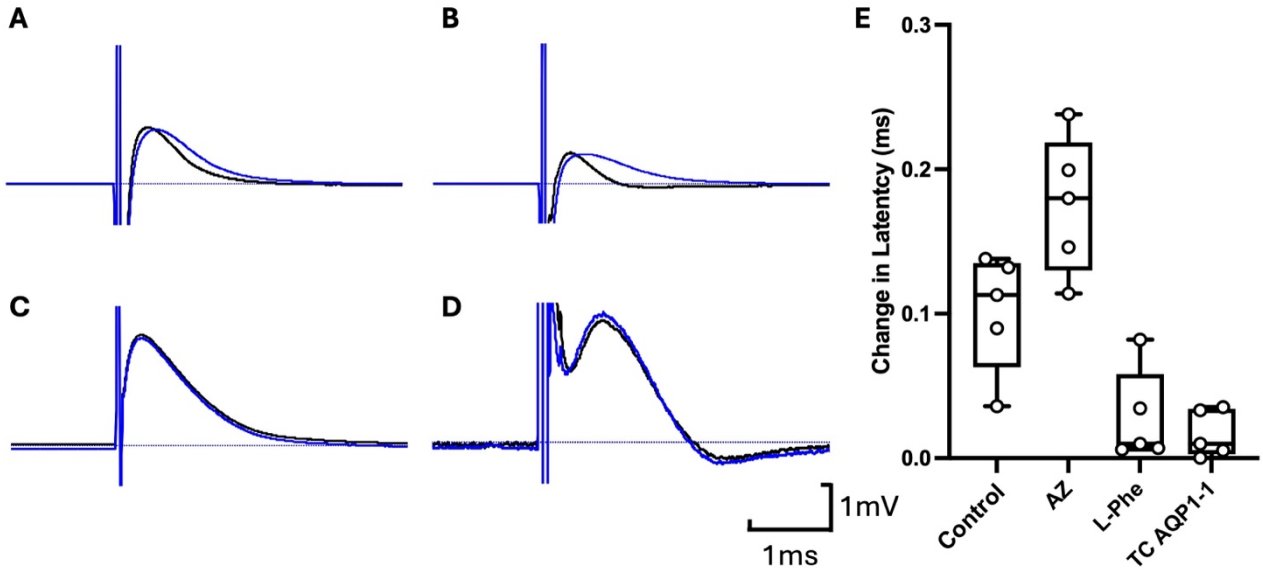

Figure 13. CO_2 dependent slowing of conduction velocity following high frequency stimulation. Representative CAPs from mouse sciatic nerve prior to high frequency stimulation (Black trace), and after (Blue trace) for WT nerves: A) in the absence of any compound; B) with 100 μM acetazolamide; C) with 1 mM L-Phenylalanine; D) with 80 μM TC AQP1-1. E) Boxplot showing the change in latency (time to peak of CAP) before and after high frequency stimulation for Control, Acetazolamide (AZ), L-Phe and TC AQP1-1. Kruskal Wallis ANOVA p=0.0016. Pairwise Mann Whitney U tests: control vs AZ, p=0.0317; control vs L-Phe, p=0.0159; control vs TC AQP1-1, p=0.0079.

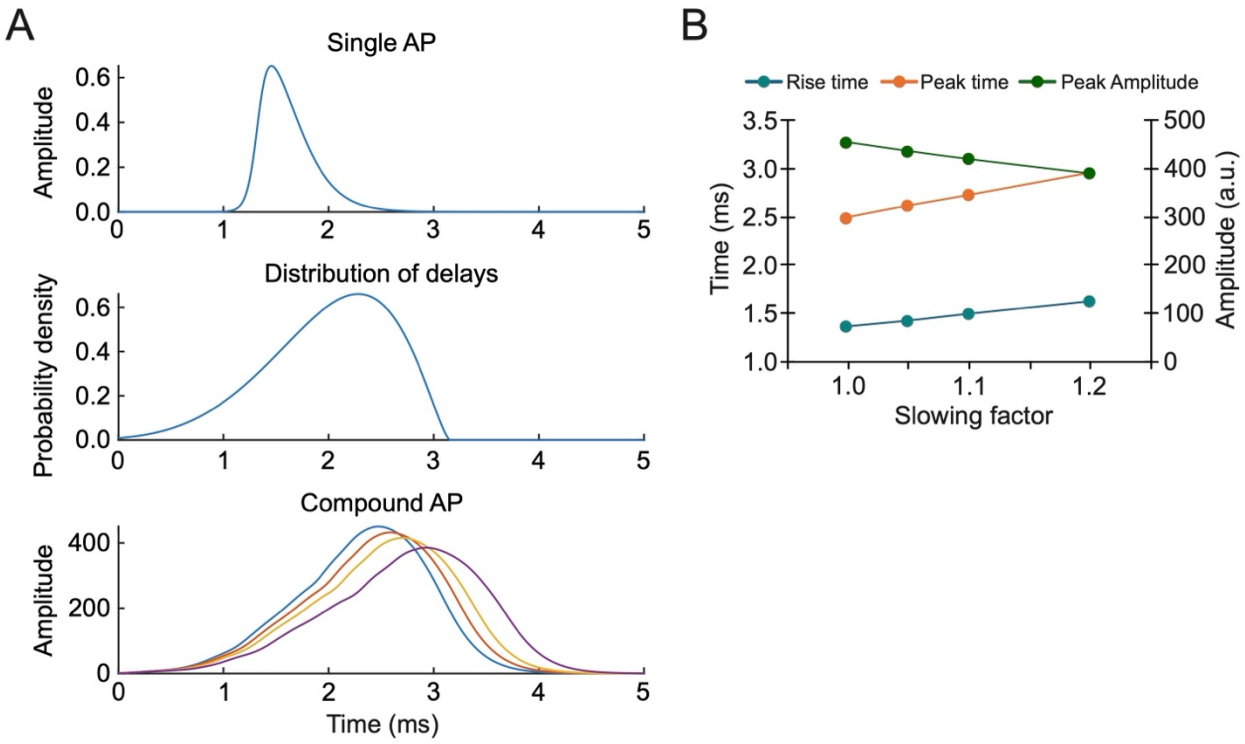

Figure 13 figure supplement 1. Model of the CAP to show how changing conduction velocity alters the rise time, time to peak and peak amplitude of the CAP. Matlab code for the model is provided in compoundAP.m.